POLITECNICO DI TORINO

Corso di Laurea Magistrale

In Ingegneria Aerospaziale

Tesi di Laurea Magistrale

Development of a numerical model for the analysis of transient phenomena in HREs

Relatori:

Prof. Dario Giuseppe Pastrone

Dott. Andrea Ferrero

Candidato:

Luca Muscarà

Ringraziamenti

Ringrazio la mia famiglia, per avermi sempre sostenuto in questo lungo percorso, per non avermi mai fatto mancare niente e per avermi costantemente incoraggiato.

Un ringraziamento speciale va alla mia Debora, per essere stata sempre presente dall'inizio di questo percorso, per avermi dato la forza quando da solo non riuscivo ad andare avanti. Se oggi sono quel che sono, se oggi sono arrivato fin qui, una buona percentuale è merito suo.

Un'altra buona percentuale è merito dei miei più cari amici. Vi ringrazio tantissimo per non aver mai smesso di credere in me.

CONTENTS

Summary

In the first chapter a history overview of the hybrid rocket engines (HREs) and their characteristic features have been exposed. In the rocket motors background the HREs exhibit several advantages over the other two configurations, the liquid rocket engines (LREs) and the solid rocket motors (SRMs). There are also some disadvantages such as the low fuel regression rate and the combustion instability. The purpose of this work is to develop a numerical method capable of observing the combustion instability in the HREs with the aid of the previous studies developed about it. In the experimental tests on the HREs, it was found that the chamber pressure increases from its mean value and it oscillates into a nonlinear limit cycle, the so-called "DC shift". Furthermore the chamber pressure oscillates with both low frequency and acoustic frequency, but the instability takes place in the low frequency regime. A well known theory was developed to study the combustion instability in the LREs and in the SRMs; unfortunately that theory can not be used in the HREs. Thus, in this thesis, it has been developed a numerical method based on three principal subsystems coupled. In detail, in the second chapter have been explained the three physical models involve in this study, in other words the quasi-one-dimensional gas dynamic model, the chemical model and the one-dimensional thermal model.

Instead, in the third chapter the numerical methods have been exposed; they were applied to solve the equations of those models. The first one is a computational fluid dynamic code in order to provide the gas dynamic properties inside the combustion chamber and the nozzle of the hybrid rocket system. Since the chemical reactions take place in the combustion chamber, a chemical code it has to be used; for this purpose it was employed the NASA CEA code [16]. Because of the complexity of the CEA code and in order to reduce the computational cost, it has been developed an additional code, later named TEST code. It takes as inputs the internal energy, density and molar fractions of the species inside the combustion chamber and provides the temperature and the pressure at the chemical equilibrium as results. Finally, the thermal conductivity of the solid-fuel has to be considered and this is possible through the solution of the heat equation by using the Finite Volume Method.

In the fourth chapter have been explained the steps in order to link this code together. The TEST code has been validated by comparing the results with the results provide

from the CEA code. Then, the TEST code has been coupled together with the CFD code. It has been studied the chemical composition in a specific nozzle configuration, before using this code to analyse the flow in the combustion chamber, and the results have been compared with the results achieved in [23]. After the validation of the code on the nozzle results available in [23], it has been extended in order to describe the flow field in the hybrid rocket engine. A further equation has been added to the fluid dynamic system so as to define the quantities of oxidizer and fuel in the mainstream. Then, the thermal code has been added and the differences between the previous version of the code has been highlighted. Finally the boundary layer delay time has been added in the code and the instability in the pressure has been made evident by comparing the results obtained between $\tau_{BL} = 0\ s$ and $\tau_{BL} = 0.001\ s$.

Chapter 1

Hybrid Rocket Engine

1.1 History of the hybrid rocket motors

Hybrid rocket propulsion systems use both liquid and solid as propellants, in detail in the classical hybrid configuration the fuel is a solid and the oxidizer is a liquid. The development of hybrid rocket engines (HREs) began in the early 1930s, also the developments of both liquid and solid rockets took place in the same time. Historically the solid rocket motors (SRMs) were first used because of a lot of knowledge in the gunpowder history. One of the problems in the SRMs was their explosive hazard, Hermann Oberth, that was one of the pioneers in rocketry, saying that: "Powder believes it must explode all at once; from the old use in shells and guns, it is too well-trained always to destroy" [1]. In the 1933 there was a tragic demonstration of those words, for this reason Robert Goddard, who had started his work with powder fuels, thought about solving the problem by injecting small quantities of powder into a small combustion chamber. His main ideas were to control burning rate avoiding the exposure of the complete fuel to the heat of the combustion.

The first forerunner to the hybrid rocket was the "Rocket Projectile No. 9", a work led by the GIRD (the Group for Investigation of Reactive Motion), the first professional rocket-development organization in the URSS [2]. That rocket was fed by the liquid oxidizer mixed with gelled gasoline, known as "solid benzene", and became known as a hybrid vehicle (although this is not the definition of a hybrid rocket). Afterward in the 1937, a lot of experiments with hybrid rockets began, but there were unsuccessful results due to the lack of knowledge in the propellants that were used. As a matter of fact, one of the main problems was the very high carbon's heat of sublimation.

Later in the mid of 1940s the Pacific Rocket Society conducted significant experiments on hybrid motors that employed LOX as oxidizer and first wood, then wax loaded in black carbon and finally rubber as fuel. The rocket was called XDF, the name comes from "experimental Douglas fir"; there were a lot of version, but the design used was the XDF-23 containing LOX rubber fuel and aluminium alloy nozzle that successfully flew in 1951 [1].

The Society worked out a fundamental result that is clear from the follow statement: " The chamber-pressure of a solid-liquid rocket engine is proportional to oxidizer flow and not to the internal surface area exposed to the flame. Thus, there is no danger of explosion due to cracks and fissures in the charge as solid propellant rockets commonly used for boosters" [3].

During the 1940s H.Bartel and W.Rannie conducted at Jet Propulsion Laboratory (JPL) the first analytical investigations of a combustion process but in a solid-fuel ramjet. In that configuration the oxidizer was air and was caught by the inlet from the atmosphere, while the solid-fuel was graphite. This particular configuration was abandoned because of the high sublimation heat of carbon; as a consequence it had not good performance in thrust level [1].

In the late 1940s analytical and experimental investigation in hybrids were conducted by George Moore and Kurt Berman at General Electric Company in Schenectady, New York. Their engine was fed by 90% of hydrogen peroxide as oxidizer and polyethylene as fuel; moreover the fuel grain was composed by a tubular or rod and tube configuration. It was discovered that with small amount of fuel added in hydrogen peroxide the features were improved in terms of specific impulse. Several tests were made and at the end they concluded that the burning was longitudinal uniform, the grain crack had no effect in terms of MEOP (Maximum Except Operator Pressure), no hard start were observed, the fuel surface behaved as its own flameholder so the combustion was stable; because of the presence of a valve in the oxidizer feeding system the throttling was fulfilled, and they also observed that a high liquid-to-solid ratio was preferable in order to achieve a uniform burning in the combustion chamber.

On the other hand they saw some negative effects; one of these was the inherent thermal instability of peroxide [4].

In the 1960's two European organizations began to work on hybrid rocket motors. These organizations were ONERA, based in France, and Volvo Flygmotor, based in Sweden. Both organizations developed sounding rockets based on hypergolic hybrid rocket motor, the first one using nitric acid as oxidizer and an amine as fuel, while the second one used polybutadiene with an aromatic amin, that it was known as " Tagaform", as fuel and also nitric acid as oxidizer. Meanwhile, other two organizations in the United States, the United Technologies Center and the Beech Aircraft, were working on a supersonic drone that it was called Sandpiper [1]. That drone was fed with MON-25

as oxidizer, in other words 25% NO and 75% N_2O_4, and with polymethyl methacrylate PMMA as a fuel.

The Sandpiper was not the only drone they tested. They developed the HAST; it had IRFNA-PB/PMM for its propellants and it could carry a heavier payload than Sandpiper.

In the mid of 1980s the Chemical System Division worked alone in a new combination of propellants for hypergolic hybrid rocket, it was used lithium and FLOx (F_2 and O_2); that combination showed good throtteable features and combustion efficiency [1].

In the late 1980s was created the largest hybrid rocket and it was made by AMROC, the American Rocket Company. The rocket was fed by LOX and hydroxyl-terminated polybutadiene (HTPB) and generated 312.000 newton of thrust for 70 seconds [1].

During the 1990s Tier One project started [5]; its aim was to allow the suborbital human spaceflight thanks to the reusable spacecraft “SpaceShipOne“ and its own launcher White Knight. The craft was designed by Burt Rutan and together with Paul Allen and Scaled Composites; they founded the Mojave Aerospace Venture to manage the commercial spinoff from the “Tier One“ [6]. The SpaceShipOne used a hybrid rocket engine supplied by SpaceDev and its propellants were liquid nitrous oxide and solid HTPB, it produced 88 kN of thrust for about 87 seconds. On June 21, 2004, the flight 15P was SpaceShipOne’s first spaceflight and the first privately funded human spaceflight, then with the flight 17P, on October 4, it won US$10 million Ansari X Prize by reaching the 112 kilometres of altitude, and it was retired in the same year [7]. The SpaceShipTwo (SS2) is the successor of SpaceShipOne, it is manufactured by the Spaceship Company. The company was founded by Burt Rutan and Robert Branson in the mid-2005, and it was owned by Virgin Group and Scaled owners. The hybrid engine has not differences from that one used in the SpaceShipOne [8]. It can be possible to recognize two engine generations, where the main difference is the fuel. The first one had a HTPB as solid-fuel but it was seen engine stability issues on burning longer than almost 20 seconds, this is the reason why the second-generation of engine used the thermoplastic polyamide as a solid fuel. However, in October 2015 Virgin Galactic announced to come back to HTPB as solid fuel [9][10].

There were also conducted experiments with the reverse configuration of hybrid rocket, where the fuel was the liquid propellant and the oxidizer was the solid propellant [1]. These experiments led to unsuccessfully results in terms of combustion behaviour and insufficient performance. Moreover this particular configuration does not concern the aim of this work and for these reasons it will not be inspected.

1.2 Advantages and disadvantages of HREs

There are many components that are common both to the liquid rocket engines (LREs) and the solid rocket motors (SRMs), but the hybrid rocket engines (HREs) present interesting advantages over them. In order to appreciate these advantages it is needed to look into the different combustion characteristics; in the solid rockets, the oxidizer and fuel are mixed in the single solid phase and the combustion occurs from a microdiffusion flame while in the liquid rockets the combustion arises from a premixed flame [11]. As a matter of fact the oxidizer and the fuel are mixed in the proximity of the injector. The hybrid, however, burns as a macrodiffusion flame where the oxidizer-to-fuel ratio O/F changes down the length of the combustion chamber, contrary to the uniform mixture in both liquid and solid rockets. This system has an inherent safety and operational features. First of all the fuel is inert and can be transported and handled safely; in addition the system does not have the risk to explode because there is not an intimate mixture of oxidizer and fuel. Unlike solid motors, in the hybrid engines it can be possible to throttle by modulating only the liquid flow rate, which is simpler than in a liquid engines where two flow rates must be synchronized; the shutdown is simply reached by turning off the liquid flow rate. The other aspect that leads to prefer hybrid engines instead of solid rockets is the grain robustness. This is due to the lack of catastrophic events when a fuel-grain crack occurs because burning happens down the port where it comes across the oxidizer flow. The selection of propellants is better than both liquid and solid. In the solid fuel, constituents can be added, such as energetic metals, to enhance performance and density, while the liquid oxidizers, in contrast to solid ones, produce higher energy levels. A common feature with the LREs and a difference with the SRMs is the temperature sensitivity. In other words the temperature effect on burn rate is small and then the temperature variations have little effect on chamber pressure. From an economical point of view the operational cost for hybrid systems is affordable and it depends on its safety features and inert propellant [1].

Despite the several advantages of hybrid systems compared to liquid and solid systems, the hybrids have not seen a mass production unlike liquid or solid, whereas they have had a famous application in the space programs. In fact, the HREs suffer from some disadvantages shown below:

- Low regression rate: the regression rate is the main parameter that embodies the HREs as the SRMs. It is the velocity with whom the solid fuel is converted into a gas fuel. Unlike the solid engine, the hybrid has a low regression rate, this influence the desire thrust level. In order to improve this parameter, the total length-to-diameter ratio L/D may be checked. This ratio has to be high especially when it requires high performance and it becomes unacceptable. One possible solution for this issue is the multiport grain, that allows to reduce L/D with an almost mass fuel grain [12]. Assuming both A_b and A_p constant, it may be reduced the length grain $L_g = A_b/P$ increasing the perimeter. Unluckily, that solution leads to other disadvantages such as the high unburned mass fraction. As a consequence of the more complicated geometries, every ports could behave in different ways, thus a dedicated injector is required. Furthermore the grain structural integrity may become an issue, especially towards the end of burning. Recently studies at Stanford University [13] suggest that paraffin-based fuels improve the regression rate reaching 3-4 times the value of a conventional hybrid fuels. The main mechanism that helps to increase the rate is the instability of a thin liquid layer produced on the grain surface. This layer is characterized by low viscosity and low surface tension; the liquid fuel droplets are injected into the boundary layer increasing the fuel mass flux and to avoid the blocking effect typical of gaseous fuel blowing.
- Mixture ratio shifting: the regression rate in HREs is assumed to be the follow semi-empirical correlation.

$$r = aG_{ox}^{n} \tag{1.1}$$

Where a and n are obtained by experimental data, and G_{ox} is the oxidizer mass flux expressed as the ratio of the oxidizer mass flow divided by the port area $G_{ox} = \dot{m}_{ox}/A_p$. During the burning, the port area increases and the regression rate decreases. On the other hand the burning area A_b increases. These two effects are not balanced and the mixture ratio shifts lead to a lower performance [12]. Because of this, unconventional injectors are required leading to a complex system.

- Mixing inefficiencies: unlike liquid or solid engines, the hybrid engines have the large diffusion flame results in a lower degree of mixing and the fuel unburned exits the nozzle before realising chemical energy. A mixer may be used to enhance the mixing but it leads to increase the dry weight of the system [12].
- Slow transient: during the course of operation HREs undergo a number of transients phenomena such as ignition or thrust response to throttling [12]. These effects are due to the thermal lag in the solid fuel and it may lead to instability phenomena that are the objects of this work.

1.3 Literature review of transient phenomena and combustion instability in HREs

During a specific mission the thrust requirements has to be followed. The transient events have to be analysed to accomplish the constraints. These events can be classified in four principal phases that are: ignition, throttling, thrust termination and combustion instability.

1) Ignition: during this process the oxidizer is heated by some kind of heat sources as spark ignition of a gaseous fuel, then the flame takes place in the aft part of the fuel grain where the mixture ratio O/F is oxidizer rich and it reaches its steady–state configuration at the end of the transient. In hybrid rocket, the time lag required to reach the steady-state configuration is longer than that required for the solid rocket, and it's due to the delay in the combustion boundary layer and thermal lag.
2) Throttling: for the same reasons during the throttling, the change of the oxidizer mass flow leads to the adjustment of the gas velocity, the temperature and the density distribution that requires a lag time to achieve to the new equilibrium.
3) Thrust termination: in hybrid rocket during the shutdown there is a relaxation period where the accumulated heat in the solid is transferred in the surface, leading to vaporization that can contribute with additional impulse. The response during this phase is essentially the emptying time of the motor, but the relaxation time is slower than emptying time and because of this it controls the shutdown impulse.

4) Combustion instability: this transient phenomenon is the argument of this work. “The instability is defined as the operation condition when the chamber pressure oscillates in a recognizably coherent form with an amplitude of at least 5% of its mean value“ [1]. It is clear that for a good design and in order to respect the mission constrains a combustion stability is needed, and it is important to understand the mechanism related to that instability. In liquid or solid engines it was developed a theory to analyse the instability phenomena but it can’t be used in HREs. The reason is to search into the regression rate law; in the SRMs the regression rate is proportional to the chamber pressure while in the HREs is proportional to the oxidizer mass flow. Although the instability mechanism and the transient events have not been explored in the most experimental tests, it has seen that the instability is in the form of limited cycle oscillations in the range of low frequencies much smaller than the first longitudinal acoustic mode of the combustion chamber. Moreover the hybrids do not have the catastrophic instabilities of liquid or solid engines; nevertheless this pressure oscillation could yield to overcome the structural loading or thermal loading. Because of this it is necessary to develop a model to predict this instability.

Several studies have been conducted and a possible theory is the thermal-combustion coupled model (TC), in this theory two transient phenomena are put together, the thermal lag in the solid fuel and the gas-phase combustion. Karabeyoglu et Al. [14] have included in the TC model another subsystem that is the gas-dynamic model (TCG). Although the TC model is good to predict the low frequency instability it is not able to provide the necessary parameters to evaluate the performance of rockets such as pressure or specific impulse. First of all they analysed every single subsystem, in particular the ignition and vaporization subsystems are not treated because there are several different elements for every design and this could lead to different response. Nevertheless these subsystems are isolated from the combustion chamber, the assumption to neglect them is valid. There are only three subsystems to take into account and they are the three involves in the TCG model.

The thermal lag model explains the delay time due to the heat capacity of the solid-fuel and because of this the regression rate can not modify instantaneously to changes in wall heat flux; in this model are also modelled the gasification and pyrolysis reactions at the surface. The second model, the gas-phase model, aims to explain what happened in a transient when changing in the oxidizer mass flow occurs. Switching the value of the

oxidizer mass flow, the turbulent boundary layer develops over the fuel surface within the chemical reactions take place. During the transient, the convective heat transfer to the surface is related to the regression rate through the blocking effect due to the blowing of the gas. These dynamics together with the thermal lag lead to the instability oscillation, Karabeyoglu et Al. [14] believe that the coupling of three parameters are responsible for the instability; these parameters are the activation energy, the blocking factor and the delay in the boundary layer dynamic. The figures below show the consequence of changing these parameters, in particular they found out that the activation energy and the blocking factor do not affect the frequency of the oscillation but they affect the amplitude. It is different from the boundary layer delay time, in fact it affects the frequency.

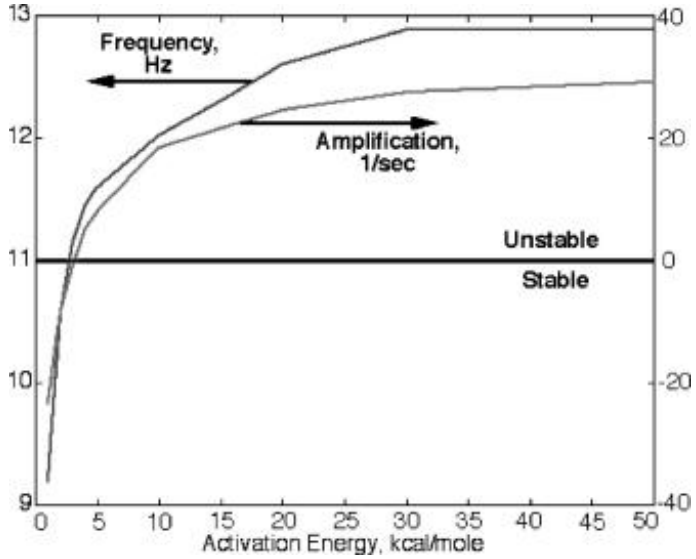

Figure 1.1. Oscillation frequency and amplitude changing the activation energy [14]

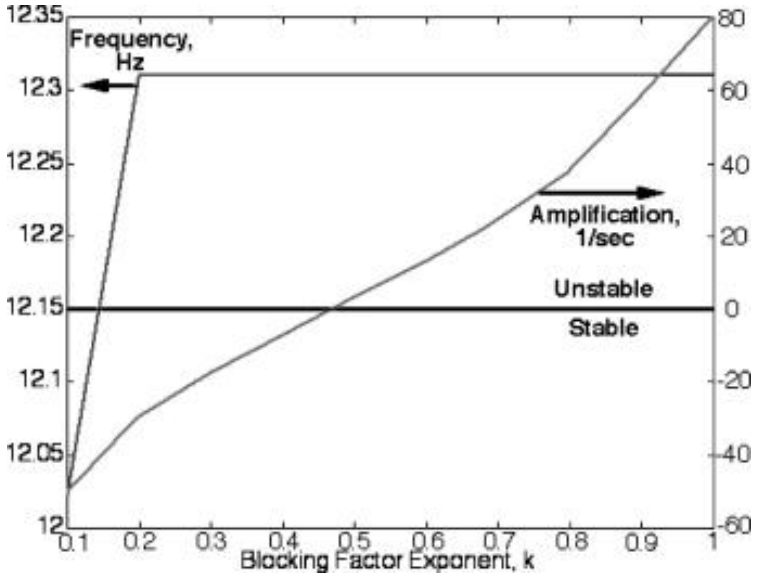

Figure 1.2. Oscillation frequency and amplitude changing the blocking factor [14]

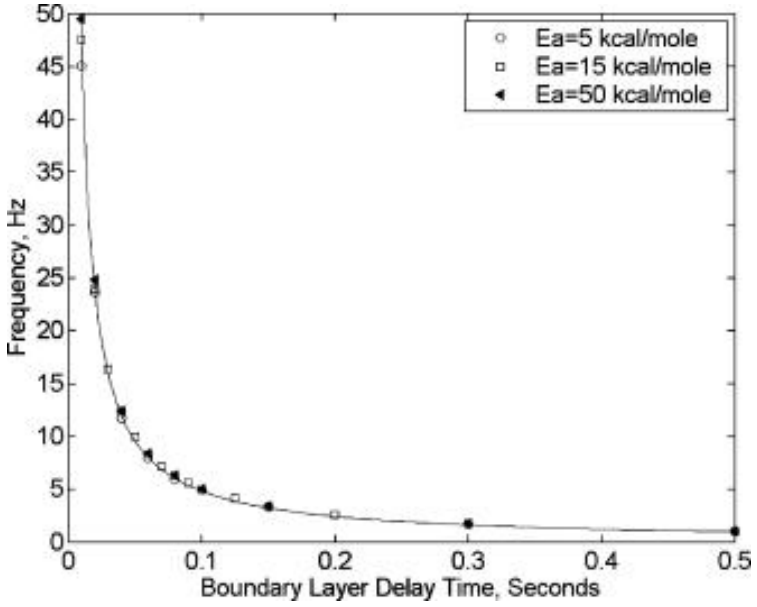

Figure 1.3. Oscillation frequency changing the boundary layer delay time [14]

In the figure 1.3, the curve-fit equation suggests a relation between the frequency and the boundary layer delay time:

$$f = \frac{0.48}{\tau_{bl}} \tag{1.2}$$

The last subsystem is the gas-dynamic model which provides the chamber pressure and the other characteristic parameters such as specific impulse and oxidizer to fuel ratio. In the paper [14] the combustion chamber is divided in three parts, pre-combustion chamber, post-combustion chamber and fuel port volume.

They treated the first two parts as zero-dimensional volume elements but they take into consideration the variations of the conservative variable along the longitudinal axis. Solving analytically the conservative laws after linearization, they obtained the transfer function for the gas dynamic model. The longitudinal modes and the filling/emptying mode are shown and no instability modes are captured. In the figure 1.4 that modes can be seen. The conclusion was that gas-dynamic model does not influence the instability dynamic, even if the presence of the boundary layer delay time.

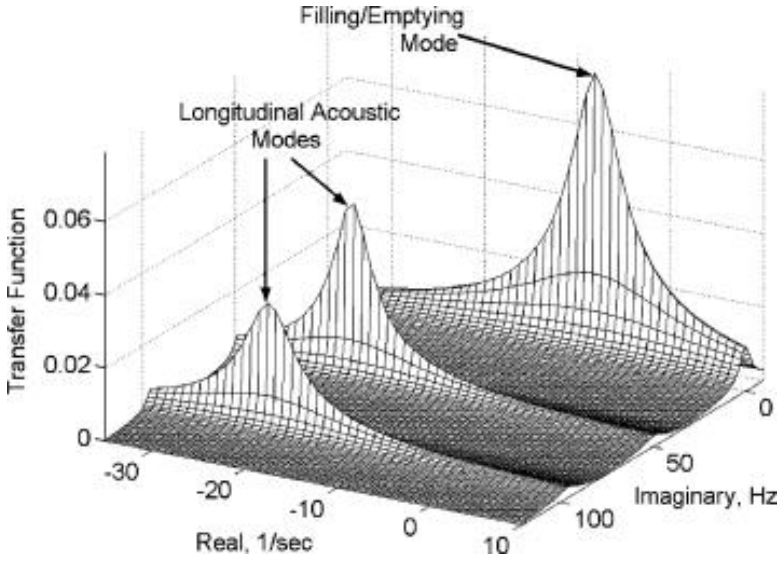

Figure 1.4. Transfer function for gas-dynamic model [14]

In the TC model only the fuel mass flux oscillation or the regression rate oscillation are represented as results. It takes the fuel mass flux and the oxidizer mass flux as inputs including the gas-dynamic model and it shows the pressure oscillation as a result. In the figure 1.5 is shown a schematic diagram flux of the TCG coupled system. In their research Karabeyoglu et Al. [14] discovered that the presence of the gas-dynamic model does not influence neither the frequency nor the amplitude of the oscillation predicted by the TC coupled system.

The figure 1.6 and 1.7 show the chamber pressure oscillation and the fast Fourier transform of chamber pressure for the paraffin-based motor tested in the Hybrid Combustion Facility at NASA Ames Research Center.

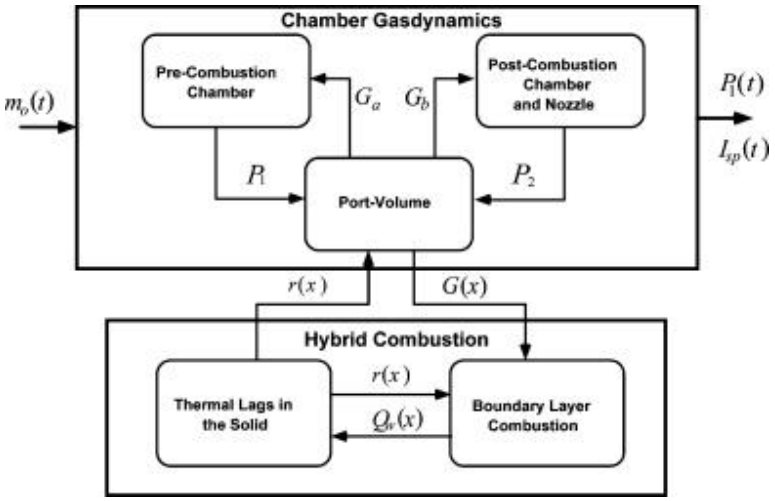

Figure 1.5. Diagram TCG coupled system [14]

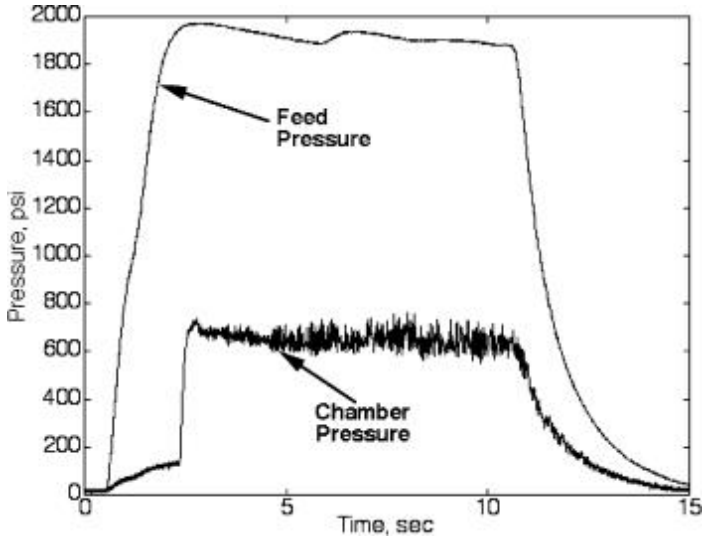

Figure 1.6. Chamber and feed pressure oscillations for paraffin-based motor [14]

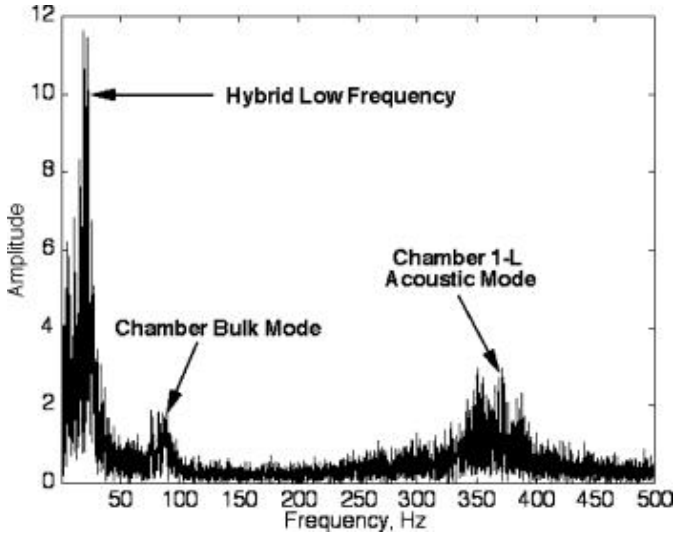

Figure 1.7. Fast Fourier Transform of chamber pressure for paraffin-based motor [14]

The fast Fourier transform of chamber pressure shows three different pick related to three different modes: the hybrid low frequency instability, the chamber bulk mode or Helmotz mode and the first longitudinal mode. It shows also that the maximum amplitude pick is reached only from the low frequency mode, while the other two modes present lower amplitude. Furthermore it is believed that the acoustic wave is driven by the low frequency instability; the variation in the oxidizer mass flux excites the acoustic modes but they decay in a short time thanks to their stability.

The TCG model is able to predict the frequency of the instability mode but it does not provide a correct result from the amplitude of this mode. It predicts infinite amplitude while it is known by the several tests that these oscillations are closed to a limit-cycle.

In the paper [15] Kung-Su Park and Changjin Lee deal with the same problem in laboratory-scale hybrid motors. They tested 15 hybrid motors changing some critical parameters such as the volume ratio; in other words they changed the ratio between the post-chamber length and the chamber length, the oxidizer mass flow rate and the type of solid fuel. In their tests they found out that the material property like the type of fuel propellant and the change in the oxidizer mass flow rate do not seem to influence the LFI, while this seems to appear when the volume ratio changes and when the fuel port diameter approaches certain values.

These and other articles are used as a reference in this thesis, especially the subsystems division in order to develop a numerical method capable of providing these transient phenomena. The physical and the numerical models will be explained in detail in the next chapters.

Chapter 2

Physical models

The physical models used to analyse the transient phenomena of the HREs will be exhibited in this chapter. It is needed to divide the physical models in order to study the fluid dynamic properties of the mixture inside the combustion chamber and the nozzle. The three models are the quasi-one-dimensional gas dynamic model, the chemical model and the thermal model.

2.1 Quasi-one-dimensional gas dynamic model

The gas dynamic model is the quasi-one-dimensional model and it is based on the Euler equations along the longitudinal axis. The model is quasi-one-dimensional because it takes into consideration the area average value and the fluid dynamic variable along the longitudinal direction. Throughout the combustion process, the fuel pass through the solid-phase into the gas phase; therefore the fuel mass flux is radially injected inside the combustion chamber. So as to consider this, a source mass is added in the Euler equations. Moreover a further equation is introduced, "the mixture fraction transport equation", as it has done by Karthikeyan, G. and Shimada T. in [11]. This equation is similar to the mass conservation equation, but in addition, there is a new variable that multiplies the density, called the "mixture fraction".

$$\epsilon = \frac{b_c - b_{c,2}}{b_{c,1} - b_{c,2}} \tag{2.1}$$

In the equation 2.1, ϵ represents the mixture fraction, while $b_{c,1}$ and $b_{c,2}$ are the mole numbers of atomic Carbon per unit mass of mixture gas inside both fuel and oxidizer. In this hybrid rocket engine model, the oxidizer is gaseous oxygen and it does not include any carbon atoms; as a matter of fact $b_{c,2}$ is equal to zero and the mixture fraction can be expressed in this way:

$$\epsilon = \frac{b_c}{b_{c,1}} \tag{2.2}$$

The standard Euler equations are modified because of the mixture fraction transport equation, the source mass and the area average value into the following equations.

$$\frac{\partial A\rho}{\partial t} + \frac{\partial A\rho u}{\partial x} = \dot{m}_f l_p \tag{2.3}$$

$$\frac{\partial A\rho u}{\partial t} + \frac{\partial A(\rho u^2 + p)}{\partial x} = p\frac{dA}{dx} \tag{2.4}$$

$$\frac{\partial A\rho E}{\partial t} + \frac{\partial A(\rho E + p)u}{\partial x} = \dot{m}_f l_p h_w \tag{2.5}$$

$$\frac{\partial A\rho \epsilon}{\partial t} + \frac{\partial A\rho \epsilon u}{\partial x} = \dot{m}_f l_p \tag{2.6}$$

In the equations above, l_p represents the perimeter of the cross-section area of the fuel grain, while h_w represents the specific enthalpy of the fuel gas evaporating from the fuel surface. The specific total energy is expressed as:

$$E = e_i + \frac{u^2}{2} \tag{2.7}$$

The parameter e_i is the specific internal energy and it is one of the inputs for the chemical model. Once the specific total energy is known, with the equation 2.7, the specific internal energy can be extracted.

In order to study the properties of the fluid dynamic equations, they can be rewritten in a compact form.

$$\frac{\partial A\bar{U}}{\partial t} + \frac{\partial A\bar{F}}{\partial x} = \bar{S} + \bar{S}_f \tag{2.8}$$

where:

$$\bar{U} = (\rho, \rho u, \rho E, \rho \epsilon)^T \tag{2.9}$$

$$\bar{F} = (\rho u, \rho u^2 + p, (\rho E + p)u, \rho \epsilon u)^T \tag{2.10}$$

$$\bar{S} = \left(0, p\frac{dA}{dx}, 0, 0\right)^T \tag{2.11}$$

$$\bar{S}_f = \left(\dot{m}_f l_p, 0, \dot{m}_f l_p h_w, \dot{m}_f l_p\right)^T \tag{2.12}$$

Generally the standard Euler equations, in their non-conservative form, may be expressed in terms of a, u and S:

$$\frac{\partial}{\partial t}\begin{Bmatrix} a \\ u \\ S \end{Bmatrix} + \begin{bmatrix} u & \delta a & 0 \\ \frac{a}{\delta} & u & -\frac{a^2}{\gamma R} \\ 0 & 0 & u \end{bmatrix} \frac{\partial}{\partial x}\begin{Bmatrix} a \\ u \\ S \end{Bmatrix} = 0 \tag{2.13}$$

The properties of the standard Euler equations are studied by using a model equation.

$$\frac{\partial \overline{V}}{\partial t} + \boldsymbol{A}\frac{\partial \overline{V}}{\partial x} = 0 \tag{2.14}$$

Where $\overline{V}$ is a vector and $\boldsymbol{A}$ is a matrix.

The equation above is a partial differential equation, precisely a hyperbolic differential equation and it represents a generalization of the advection equation $\left(\frac{\partial u}{\partial t} + a\frac{\partial u}{\partial x} = 0\right)$. For this type of equation exists a technique to solve it, the method of characteristic. This method is to transform the PDE in a system of ODE and to find the characteristic curve, along which signals are propagated (as example $u(x,t)$ for advection equation), but its derivatives are not defined. Therefore, if you know the initial conditions, it will be simple to solve the solution in the simple case of the 1D advection equation; because the solution, at a certain time and space, propagates through a characteristic line with constant slope a. This slope may be not constant if a is a function of the solution. This is the case of the equation 2.14, where the slope is a function of the solution; moreover, there are three characteristic curves and their slopes that can be found by solving the determinant of the matrix $[A - \lambda I]$. The three slopes of the characteristic curves are the following:

$$\Lambda_1 = u - a \tag{2.15}$$

$$\Lambda_2 = u \tag{2.16}$$

$$\Lambda_3 = u + a \tag{2.17}$$

It is not enough to know the initial conditions in order to solve the PDE, but it is needed also to known the boundary conditions. The characteristic method, thanks to the slopes of the characteristic curves, helps to choose where and how many boundary conditions

have to be imposed. In the standard Euler equations, the slopes of the characteristic curves, depends on the Mach number of the flow field; indeed, if the flow field is in the supersonic regime all the three curves have positive slopes in the time-space plane. It is different from the subsonic regime, because one of the three characteristic curves has a negative slope in the time-space plane.

In a one-dimensional problem, as that treated in this thesis, if the flow is supersonic at the inlet, then three boundary conditions have to be imposed; while, if it is subsonic, then only two boundary conditions have to be imposed, but they must be able to communicate with the characteristic curve coming from within the domain. In the outlet of the domain, in the same way, if the flow is supersonic, then no boundary conditions have to be imposed; otherwise, if the flow is subsonic, only one boundary condition is needed.

In this thesis, the flow is subsonic at the inlet, but becomes supersonic at the outlet; so the boundary conditions are imposed only at the inlet.

2.2 Chemical equilibrium model

The gas dynamic model itself is not able to capture the correct thermodynamic features of the mainstream flow into the combustion chamber, because a chemical reaction occurs. Therefore a chemical model is required. Since the time scale of the chemical kinetics is lower than the fluid dynamic time scale, it can be possible to consider the chemical equilibrium model without introducing a significant error. The numerical code applied to resolve the chemical equilibrium is the CEA code [16], it uses a solution method based on the minimization of free energy. The free energy could be the Gibbs energy or the Helmhotz energy, it depends on the thermodynamic state variable. The variation of the free energy have to be zero, this is the condition for the chemical equilibrium. What energy has to be selected, Gibbs or Helmhotz energy, depends on which thermodynamic variables are chosen to characterize the thermodynamic state.

Before describing how this method works, it is necessary to introduce some assumptions. All the gases are considered ideal, therefore the equation state for the mixture is:

$$\frac{p}{\rho} = nRT \tag{2.18}$$

where n is the number of moles per kilogram of mixture, it is not constant during the reaction. The equation 2.18 is supposed to be correct even if the condensed species are present. The variables ρ or V and n refer to gaseous species, while the mass of the mixture refers to every species that are included in the reaction products. As a consequence, the following relation can be written:

$$n = \sum_{j=1}^{NG} n_j \tag{2.19}$$

where n_j is the number of moles of the j-th species per kilogram of mixture and NG is the number of the gaseous species in the mixture.
The molecular weight of the mixture is expressed as:

$$M = \frac{1}{n} \tag{2.20}$$

or

$$M = \frac{\sum_{j=1}^{NS} n_j M_j}{\sum_{j=1}^{NG} n_j} \tag{2.21}$$

In the equation 2.21 M_j is the molecular weight of the j-th species, while NS refers to all the species in the mixture. It should be noted that the CEA code considers from 1 to NG only the gaseous species and from $NG + 1$ to NS the condensed species.

2.2.1 Minimization of Gibbs energy

The Gibbs energy is a state function. It represents the free energy in the thermodynamic state with constant temperature and pressure. These two state variables are the Gibbs energy own natural variables; as a matter of fact it is used to solve the chemical equilibrium when temperature and pressure are assigned. The definition of that energy is:

$$g = h - Ts \tag{2.22}$$

It also has another definition based on the chemical potential. In fact in a NS species mixture the Gibbs energy is better defined as:

$$g = \sum_{j=1}^{NS} \mu_j n_j \tag{2.23}$$

The classical definition of the chemical potential of the *j*-th species is shown in the equation 2.24.

$$\mu_j = \left(\frac{\partial g}{\partial n_j}\right)_{T,P,n_{i\neq j}} \tag{2.24}$$

As the Gibbs energy, also for the specific enthalpy and for the specific entropy of the mixture, there are definitions based on the number of species.

$$h = \sum_{j=1}^{NS} n_j H_j^{\circ} \tag{2.25}$$

$$s = \sum_{j=1}^{NS} n_j S_j \tag{2.26}$$

In the equations 2.25 and 2.26, H_j° is the standard-state molar enthalpy of the *j*-th species of the mixture and S_j is the entropy of the *j*-th species of the mixture. As well as the chemical potential μ_j, also the entropy S_j has different relations in order to distinguish it from gaseous and condensed species, and these relations are written below.

$$\mu_j = \begin{cases} \mu_j^{\circ} + RTln\left(\frac{n_j}{n}\right) + RTlnP & j = (1, \dots, NG) \\ \mu_j^{\circ} & j = (NG+1, \dots, NS) \end{cases} \tag{2.27}$$

$$S_j = \begin{cases} S_j^{\circ} - Rln\left(\frac{n_j}{n}\right) - RlnP & j = (1, \dots, NG) \\ S_j^{\circ} & j = (NG+1, \dots, NS) \end{cases} \tag{2.28}$$

In 2.27 and 2.28, μ_j° is the standard-state chemical potential and S_j° is the standard-state molar entropy.

The minimization of the Gibbs energy is a constrained minimization problem. The constraint is the mass-balance and it may be expressed with the next equation.

$$\sum_{j=1}^{NS} a_{ij} n_j - b_i^{\circ} = 0 \quad with \quad (i = 1, \dots, l) \tag{2.29}$$

or

$$b_i - b_i^{\circ} = 0 \quad with \quad (i = 1, \dots, l) \tag{2.30}$$

In equation 2.29, a_{ij} represents the stoichiometric coefficients; in other words, the number of atoms of element *i* per mole of species *j*, and b_i° is the assigned number of atoms of the *i*-th element per kilogram of the reactants mixture. The parameter b_i, in equation 2.30, is the number of atoms of the *i*-th element per kilogram of the products mixture, it may be written as the following:

$$b_i = \sum_{j=1}^{NS} a_{ij} n_j \quad with \quad (i = 1, \dots, l) \tag{2.31}$$

In order to solve the constrained minimization problem, the method of Lagrange multipliers is applied. Instead of the Gibbs energy, a new function is minimized. This function takes into consideration the mass-balance constraint.

$$G = g + \sum_{i=1}^{l} \lambda_i (b_i - b_i^{\circ}) \tag{2.32}$$

The equation 2.32 can be differentiated and set equal to zero for the equilibrium problem.

$$\delta G = \sum_{j=1}^{NS} (\mu_j + \sum_{i=1}^{l} \lambda_i a_{ij}) \delta n_j + \sum_{i=1}^{l} (b_i - b_i^{\circ})\, \delta \lambda_i = 0 \tag{2.33}$$

Treating separately δn_j and $\delta \lambda_i$ lead to two equations; one of these is the mass balance equation 2.33, while the other is a new equation 2.34, that links the chemical potential with the stoichiometric coefficients.

$$\mu_j + \sum_{i=1}^{l} \lambda_i a_{ij} = 0 \;\; with \quad (j = 1, \dots, NS) \tag{2.34}$$

The chemical equilibrium problem can be solved with the aid of the equations 2.25 and 2.26 once assigned two thermodynamic state variables. As discussed previously, temperature and pressure are usually assigned ($T = T_o; P = P_o$), but also enthalpy and pressure ($h = h_o; P = P_o$) or entropy and pressure ($s = s_o; P = P_o$) may be assigned. This adds other two equations. Furthermore the equations system for the equilibrium

problem is not linear in the composition variables, this requires an iterative procedure. This procedure will be explained later on the paragraph 3.4.

2.2.2 Minimization of Helmhotz energy

As well as the Gibbs energy, also the Helmhotz energy is a state function, but it is defined in a different way. The equations below are the expression of the Helmhotz energy, and they show the connection with the Gibbs and with the chemical potential. In equation 2.37 the definition of the chemical potential is different from the equation 2.24. Diversely from the Gibbs energy, the Helmhotz energy is used to solve the equilibrium problem with constant temperature and volume; as a consequence there is the volume instead of the pressure in the subscripts of the equation 2.37.

$$f = g - pV \tag{2.35}$$

$$f = \sum_{j=1}^{NS} \mu_j n_j - pV \tag{2.36}$$

$$\mu_j = \left(\frac{\partial f}{\partial n_j}\right)_{T,V,n_{i\neq j}} \tag{2.37}$$

In addition, the chemical potential is defined according to the phase of the species.

$$\mu_j = \begin{cases} \mu_j^{\circ} + RT \ln \frac{n_j R' T}{V} & j = (1, \dots, NG) \\ \mu_j^{\circ} & j = (NG+1, \dots, NS) \end{cases} \tag{2.38}$$

where $R' = R \times 10^{-5}$ according to [16].
Substituting the equation 2.22 in 2.35 it can obtain the following:

$$f = h - Ts - PV = e - Ts \tag{2.39}$$

As well as the specific enthalpy h, also the specific internal energy e is function of n_j and it can be seen below:

$$e = \sum_{j=1}^{NS} n_j E_j^{\circ} \tag{2.40}$$

The minimization of the Helmhotz energy is also a constraint minimization problem. It can be defined a new function with the Lagrangian method and sets the condition for the equilibrium, as shown before for the Gibbs energy.

$$F = f + \sum_{i=1}^{l} \lambda_i (b_i - b_i^{\circ}) \tag{2.41}$$

$$\delta F = \sum_{j=1}^{NS} (\mu_j + \sum_{i=1}^{l} \lambda_i a_{ij}) \delta n_j + \sum_{i=1}^{l} (b_i - b_i^{\circ})\, \delta \lambda_i = 0 \tag{2.42}$$

Treating δn_j and $\delta \lambda_i$ independently, it can be found the following equation:

$$\mu_j + \sum_{i=1}^{l} \lambda_i a_{ij} = 0 \;\; with \;\; (j = 1, \dots, NS) \tag{2.43}$$

This equation is apparently equal to the equation 2.34, the difference is on the definition of the chemical potential. Moreover, other two equations are needed to solve the problem and they are found by imposing the two thermodynamic state variables; these variables could be temperature and volume ($T = T_o; V = V_o$), specific internal energy and volume ($e = e_o; V = V_o$) or specific entropy and volume ($s = s_o; V = V_o$). The set of equations are not linear in the concentration variables as the equations for the minimization of the Gibbs energy.

2.3 One-dimensional thermal model

In the quasi-one-dimensional gas dynamic model is present the source term, in which there is the fuel flow rate $\dot{m}_f$ and it is evaluated as the product between the fuel density ρ_f and the regression rate $\dot{r}$. It is not simple to calculate $\dot{r}$ because it depends on the wall temperature at the fuel surface. In order to obtain this parameter a thermal model is required.

The one dimensional heat conduction equation is used to describe the temperature profile inside the solid-fuel and to give the wall temperature that is needed to evaluate the regression rate. Some assumptions have to be done and according to [17], they are:

- The thermal penetration thickness is much smaller than the fuel port grain, this enables to solve the problem in a planar coordinate system.

- The thermo-physical properties of the solid-fuel are assumed to be constant with the temperature.
- The reaction and melting of the solid-phase are confined inside the thin layer below the regression surface.

The figure 2.1 shows the schematic temperature profile inside the flame and the fuel grain, the direction of the heat transfer, the fuel flow rate and the regression rate.

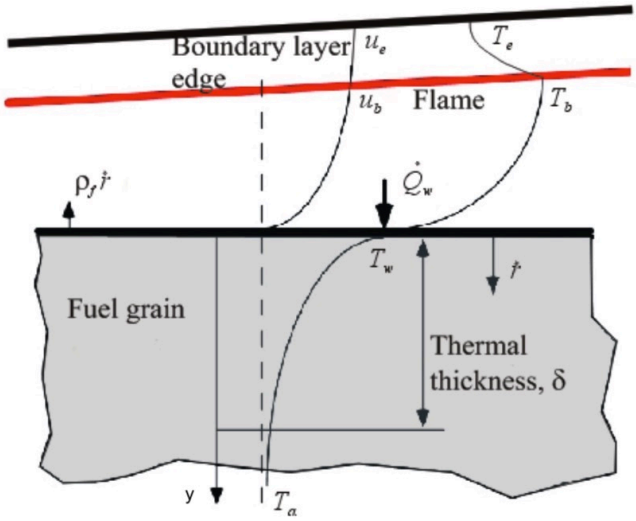

Figure 2.1. Schematic temperature profile inside the flame and the fuel-grain [17]

In the following equation it is shown the one-dimensional heat conduction equation with a reference system which follows the moving regression surface.

$$\frac{\partial T}{\partial t} = \dot{r}\frac{\partial T}{\partial y} + \alpha\frac{\partial^2 T}{\partial y^2} \tag{2.44}$$

The parameter α is the solid thermal diffusivity and it is calculated as $\alpha = \frac{k}{\rho_f c_p}$, where k is the thermal conductivity and c_p is the specific heat capacity at constant pressure.
The equation 2.44 is a partial differential equation, so the boundary and the initial conditions have to be specified in order to find the solution. The first boundary condition is the following:

$$x \to \infty \qquad T = T_a \tag{2.45}$$

The second boundary condition is imposed at the wall position, and it is:

$$x = 0 \qquad \dot{Q}_w = -k\left(\frac{\partial T}{\partial y}\right)_w + \dot{r}\rho_f L_v \tag{2.46}$$

Where L_v is the heat of vaporization and $\dot{Q}_w$ is the heat exchanged to the wall. This boundary condition says that the heat exchanged to the wall is equal to the heat lost by conduction and the heat required to vaporize the solid [17].
The other condition is the initial condition that imposes a certain initial temperature distribution inside the solid-fuel. It is expressed as the following:

$$t = 0 \qquad T(y) = T_i(y) \tag{2.47}$$

A law for the regression rate is necessary to close the problem. The Arrhenius type relation is used to approximate the pyrolysis or the vaporization process; this relation links the regression rate with the wall temperature as it can see below:

$$\dot{r} = A_h e^{-\frac{E_a}{RT_w}} \tag{2.48}$$

In that relation appears three parameters: A_h that is a pre-exponential constant, E_a that is the activation energy and $\tilde{R}$ that is the specific gas constant.

2.3.1 Wall heat flux model

In the equation 2.46 the wall heat flux refers only to the convective heat flux and it has to be defined. Starting from the assumption of Marxman and Gilbert [18], the flow through the grain surface is schematized as a turbulent boundary layer. Furthermore, the flame is placed at a distance where the oxidizer to fuel ratio is almost stoichiometric.
Therefore, the wall heat flux is expressed as a function of the Stanton number St that takes into consideration the flame properties.

$$\dot{Q}_w = St\rho_b u_b \Delta h \tag{2.49}$$

The subscript b refers to the flame and Δh is the difference between the enthalpy at the flame and the enthalpy at the wall in the gas phase. In the presence of combustion or

blowing the transition from laminar to turbulent boundary layer takes place at smaller Reynolds number then in the absence of blowing or combustion. Under the assumption that over the whole combustion chamber the turbulent boundary layer is developed, it is possible to link the Stanton number with the skin friction coefficient.

$$St = \frac{1}{2} C_f \left(\frac{\rho_e u_e^2}{\rho_b u_b^2} \right) \implies \dot{Q}_w = \frac{1}{2} C_f G \left(\frac{u_e}{u_b} \right) \Delta h \tag{2.50}$$

In the equation 2.50 C_f is the skin friction coefficient, u_e refers to the velocity at the boundary layer edge and $G = \rho_e u_e$ is the total mass flux.

An important phenomenon is the "blocking-effect"; it is due to the vaporization of the fuel mass, this effect must be considered because it influences directly the wall heat flux and the regression rate. When the regression rate is high, the wall-heat flux decreases due to the blowing of the gas-fuel, but this reduction in the wall-heat flux consequently implies a reduction in the regression rate and the blowing. This is an oscillatory mechanism that affects the transition-state during the combustion. In order to take this effect into account, the dimensionless blowing parameter is used and it is defined as the following:

$$B = 2\rho_f \dot{r} / G C_f \tag{2.51}$$

Marxman [19] found a relationship between the skin friction coefficient C_f and the skin friction coefficient C_{f0} in the absence of the blowing. He started from the relation proposed by Lees, where the "blocking-effect" is evaluated from the "film-theory" approach.

$$\frac{C_f}{C_{f0}} = \frac{\ln(1+B)}{B} \tag{2.52}$$

The equation 2.52 does not consider the effect of the wall-mass injection. Therefore, Marxaman proposed a new expression for $\frac{C_f}{C_{f0}}$ that is able to account the increase of the boundary layer thickness when the wall-mass injection or B is large.

$$\frac{C_f}{C_{f0}} = \left[\frac{\ln(1+B)}{B}\right]^{0.8} \left[\frac{\left(1+\frac{13B}{10}+\frac{4B^2}{11}\right)}{(1+B)\left(1+\frac{B}{2}\right)^2}\right]^{0.2} \tag{2.53}$$

In the range $5 \leq B \leq 100$ the equation 2.51 is approximated with the following equation:

$$\frac{C_f}{C_{f0}} = qB^{-k_b} \tag{2.54}$$

Furthermore if $B \to 0$, the equation 2.52 provides non-physical results, thus, in this case an alternative equation is proposed, according to [17].

$$\frac{C_f}{C_{f0}} = \frac{1}{1+0.4B} \tag{2.55}$$

The parameters q and k_b are imposed to be $q = 1$ and $k_b = 0.68$, but with that value of q the equation 2.52 and 2.53 do not match. In order to avoid that problem D. Pastrone and C. Carmicino in [17] found the value of q such that the two equations are equal.

$$q = \frac{B^{*k_b}}{1+0.4B^*} \tag{2.56}$$

Where B^* is the value of B for the equivalence of the equations.
Moreover, by taking the derivative of the difference between equation 2.52 and 2.53 and equating it to zero, they found the following value for q and B^*:

$$q = \left(2.5\frac{k}{1-k}\right)^k (1-k) \tag{2.57}$$

$$B^* = 2.5\frac{k}{1-k} \tag{2.58}$$

Substituting equation 2.55 in 2.51 for $B \leq B^*$, the following relation for the blowing parameter is obtained:

$$B = \frac{2\rho_f \dot{r}}{GC_{f0} - 0.8\rho_f \dot{r}} \tag{2.59}$$

While substituting equation 2.54 in 2.51 for $B > B^*$, another relation for B is expressed below.

$$B = \left(\frac{2\rho_f \dot{r}}{0.996 G C_{f0}}\right)^{\frac{1}{1-k}} \tag{2.60}$$

The wall-heat flux can be rewrite including the thermochemical blowing parameter $B_t = \left(\frac{u_e}{u_b}\right) \Delta h / h_v$, with $h_v = L_v + c_p(T_w - T_a)$.

$$\dot{Q}_w = \frac{1}{2} C_f \frac{C_f}{C_{f0}} G B_t h_v \tag{2.61}$$

As a consequence also the wall-heat flux can be written with two equations based on the blowing parameter.

$$\dot{Q}_w = B_t h_v \left(\frac{1}{2} C_{f0} G - 0.4 \rho_f \dot{r}\right) \qquad if\ B \leq B^* \tag{2.62}$$

$$\dot{Q}_w = \frac{0.996}{2} C_{f0} G B_t h_v \left(\frac{2\rho_f \dot{r}}{0.996 G C_{f0}}\right)^{-\frac{k}{1-k}} \ if\ B > B^* \tag{2.63}$$

Chapter 3
Numerical methods

3.1 Finite volume method for the Euler equations

The quasi-one-dimensional gas dynamic model involves partial differential equations, so as to solve them the finite volume method is implemented. This method is preferable to the differential method because there is no need to switch from a physical plane to a calculation plane. Therefore, the physical domain is discretized with elementary volumes, but with some conditions. These conditions are:

1. The elementary volumes must not overlap;
2. Two neighbours elements must have only one side in common;
3. The elements must cover the whole physical domain;

In order to explain how this method works a compact form of the one-dimensional standard Euler equations, with the source term, is taken into considerations.

$$\frac{\partial \bar{U}}{\partial t} + \frac{\partial \bar{F}}{\partial x} = \bar{Q} \tag{3.1}$$

The schematic discretization domain in time and space are shown below.

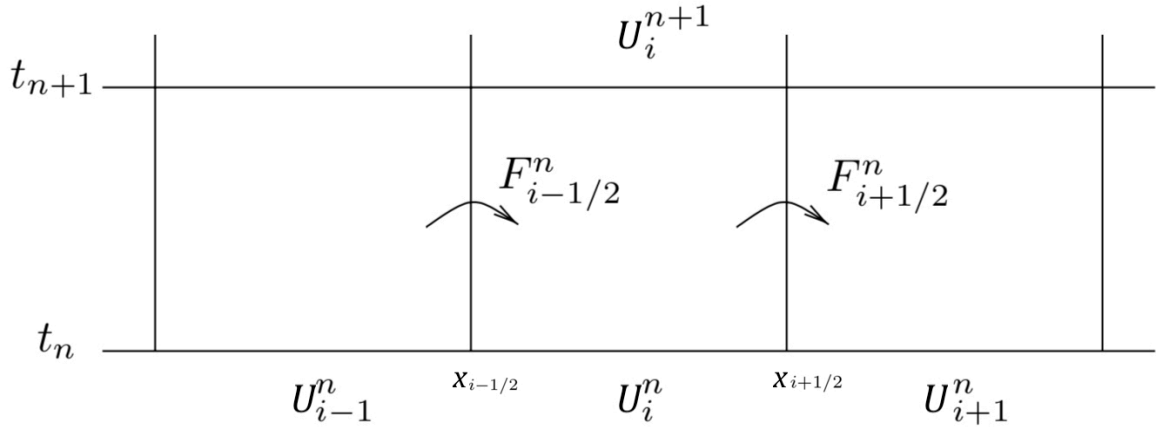

Figure 3.1. Schematic discretization one-dimensional domain in space and time [20]

The equation 3.1 can be rewritten in an integral form.

$$\frac{\partial}{\partial t}\int_{x_{i-\frac{1}{2}}}^{x_{i+\frac{1}{2}}} \overline{U}dx + \left[\overline{F}\left(\overline{U}\left(x_{i+\frac{1}{2}}, t_n\right)\right) - \overline{F}\left(\overline{U}\left(x_{i-\frac{1}{2}}, t_n\right)\right)\right] = \int_{x_{i-\frac{1}{2}}}^{x_{i+\frac{1}{2}}} \bar{Q}dx \tag{3.2}$$

The equation above is applied to every elementary volume, or grid cell, and for each of them the average values of $\overline{U}$ and $\bar{Q}$ are defined as the follows:

$$\overline{U}_i = \frac{1}{\Delta x}\int_{x_{i-\frac{1}{2}}}^{x_{i+\frac{1}{2}}} \overline{U}dx \tag{3.3}$$

$$\bar{Q}_i = \frac{1}{\Delta x}\int_{x_{i-\frac{1}{2}}}^{x_{i+\frac{1}{2}}} \bar{Q}dx \tag{3.4}$$

The average values may be associated to the centres or to the vertices of the cells. In this case the average value is associated to the centres of the cells; as a consequence the equation 3.2 becomes the following:

$$\frac{\partial(\overline{U}_i)}{\partial t} + \frac{\left(\overline{F}_{i+\frac{1}{2}} - \overline{F}_{i-\frac{1}{2}}\right)}{\Delta x} = \bar{Q}_i \tag{3.5}$$

Where:

$$\overline{F}_{i+\frac{1}{2}} \cong \overline{F}\left(\overline{U}\left(x_{i+\frac{1}{2}}, t_n\right)\right) \tag{3.6}$$

$$\overline{F}_{i-\frac{1}{2}} \cong \overline{F}\left(\overline{U}\left(x_{i-\frac{1}{2}}, t_n\right)\right) \tag{3.7}$$

The fluxes at the interface between two adjacent cells can be estimated by knowing the states of the two adjacent cells. Later it will be explain what method is used to calculate the fluxes at the interface.

3.2 Time and space discretization

The choice of the discretization scheme is important to avoid stability problems. In order to explain what is the good choice, the advection equation is considered.

$$\frac{\partial U}{\partial t} + a\frac{\partial U}{\partial x} = 0 \tag{3.8}$$

The first term of the equation is approximated with the first-order Taylor series.

$$\frac{\partial U}{\partial t} = \frac{U(x_i,t_n+\Delta t)-U(x_i,t_n)}{\Delta t} + O(\Delta t) \tag{3.9}$$

Indeed, for the second term, there are three possible schemes: the backward scheme, the forward scheme and the central scheme.

$$\text{Forward scheme} \quad \rightarrow \quad \frac{\partial U}{\partial x} = \frac{U(x_{i+1},t_n)-U(x_i,t_n)}{\Delta x} + O(\Delta x) \tag{3.10}$$

$$\text{Backward scheme} \quad \rightarrow \quad \frac{\partial U}{\partial x} = \frac{U(x_i,t_n)-U(x_{i-1},t_n)}{\Delta x} + O(\Delta x) \tag{3.11}$$

$$\text{Central scheme} \quad \rightarrow \quad \frac{\partial U}{\partial x} = \frac{U(x_{i+1},t_n)-U(x_{i-1},t_n)}{2\Delta x} + O(\Delta x^2) \tag{3.12}$$

$U(x_i, t_n)$ can be substituted with U_i^n and the advection equation may be implemented by using one of the following numerical schemes:

$$\text{Forward scheme} \quad \rightarrow \quad U_i^{n+1} = U_i^n - a\frac{\Delta t}{\Delta x}(U_{i+1}^n - U_i^n) \tag{3.13}$$

$$\text{Backward scheme} \quad \rightarrow \quad U_i^{n+1} = U_i^n - a\frac{\Delta t}{\Delta x}(U_i^n - U_{i-1}^n) \tag{3.14}$$

$$\text{Central scheme} \quad \rightarrow \quad U_i^{n+1} = U_i^n - a\frac{\Delta t}{2\Delta x}(U_{i+1}^n - U_{i-1}^n) \tag{3.15}$$

All of the three schemes are explicit schemes because the solution at a certain point in the space is evaluated from the solution at a previous time. Each type of numerical scheme must fulfill the requirements of consistency, stability and convergence. A numerical scheme is said to be consistent if it tends to the starting equation by reducing the truncation error [21]. The schemes above are all consistent with the starting equation when $\Delta t \to 0$ and $\Delta x \to 0$.

Furthermore, Lax Equivalence theorem states that for a consistent finite difference method for a well-posed linear initial value problem, the method is convergent if and only if it is stable. As a consequence, it is necessary only the stability analysis to ensure the convergence of the numerical scheme.

A numerical scheme is said to be stable if it produces a bounded error. This error is called "round-off" error and it is the difference between the numerical solution and the exact numerical solution and it depends on the machine precision.

The Von Neumann stability analysis is used to check the stability of the numerical method and it is based on the Fourier decomposition of the "round-off" error [21].

Based on the definition of "stable condition" it is possible to write the following equation.

$$U_i^n = \bar{\bar{U}}_i^n + \epsilon_i^n \tag{3.16}$$

Where $\bar{\bar{U}}_i^n$ represents the exact numerical solution and ϵ_i^n is the "round-off" error in a certain point of time and space. It can obtain the error evolution by replacing 3.16 in the three numerical schemes.

$$\text{Forward scheme} \quad \rightarrow \quad \epsilon_i^{n+1} = \epsilon_i^n - a\frac{\Delta t}{\Delta x}(\epsilon_{i+1}^n - \epsilon_i^n) \tag{3.17}$$

$$\text{Backward scheme} \quad \rightarrow \quad \epsilon_i^{n+1} = \epsilon_i^n - a\frac{\Delta t}{\Delta x}(\epsilon_i^n - \epsilon_{i-1}^n) \tag{3.18}$$

$$\text{Central scheme} \quad \rightarrow \quad \epsilon_i^{n+1} = \epsilon_i^n - a\frac{\Delta t}{2\Delta x}(\epsilon_{i+1}^n - \epsilon_{i-1}^n) \tag{3.19}$$

The "round-off" error evolution is described exactly as the numerical method, then the Fourier series is applied to this error and as a consequence the stability of each numerical method can be analysed.

To sum up, all the passages will be not explained, but only the conclusions will be exposed.

If a is positive only the backward scheme is stable, but with the condition that $a\frac{\Delta t}{\Delta x} \leq 1$, while if a is negative only the forward scheme is stable with the same condition. These types of schemes are called "Upwind" scheme, they attempt to discretize the information in the direction in which it propagates.

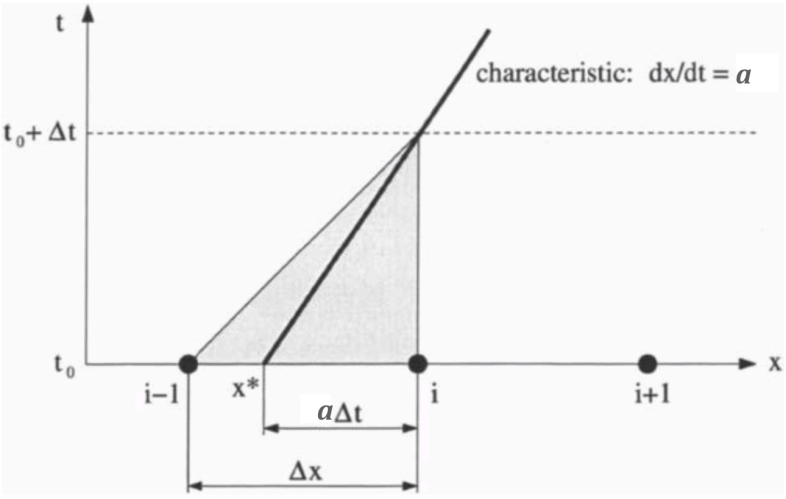

Figure 3.2. Example of Upwind discretization scheme [21]

The condition for the stability of the numerical scheme is called "the convergence condition of Courant-Friedrichs-Lewy", or simply "CFL". This condition is necessary for the stability of the explicit numerical scheme. It is based on the condition that the numerical domain must include the analytic domain, as it can be seen in the figure 3.2. In other words, it imposes a time step once the length interval is determined. In the case that a is not constant, the condition is $a\frac{\Delta t}{\Delta x} < 1$ and this is the case for the Euler equation. As regards implicit schemes, where the solution is found involving both the solution at the current time and at the later one, it is not necessary any stability condition because they are already stable. An example of implicit central scheme is shown in the following equation.

$$U_i^{n+1} = U_i^n - a\frac{\Delta t}{2\Delta x}(U_{i+1}^{n+1} - U_{i-1}^{n+1}) \tag{3.20}$$

Despite of the good stability properties, this scheme involves an extra computation. The choice between the explicit and the implicit scheme depends on the problem type. If we

are interested to study a steady-state condition, the implicit method may be the right choice, while if we want to study the transient-state, the explicit method could be used with the right condition on the time step.

The explicit central scheme, as it can be seen before with the Von Neumann analysis, is unstable, but it could be made stable by adding an artificial viscosity. This viscosity is obtained substituting U_i^n with $\frac{U_{i+1}^n+U_{i-1}^n}{2}$, the effect is to dampen the oscillations.

3.3 Fluxes discretization

The Lax-Friedrichs method is used to discretize the fluxes in the equation 3.5 [20]. This method is based on the considerations made regarding the central scheme; so an artificial viscosity is added. The new expression for the fluxes at the interface is shown below.

$$F_{i+\frac{1}{2}} = \frac{(F_i+F_{i+1})}{2} - \frac{(U_{i+1}^n-U_i^n)}{2}\max(\tilde{u}_B + a_B, \tilde{u}_A + a_A) \tag{3.21}$$

$$F_{i-\frac{1}{2}} = \frac{(F_i+F_{i-1})}{2} - \frac{(U_i^n-U_{i-1}^n)}{2}\max(\tilde{u}_B + a_B, \tilde{u}_A + a_A) \tag{3.22}$$

In the equations 3.21 and 3.22, $\tilde{u}$ and a are the flow velocity and sound speed and the subscripts, *A* or *B*, refer to the two adjacent cells.

The Lax-Friedrichs method is very dissipative due to the presence of the artificial viscosity; therefore it is able to dampen the possible oscillations. Nevertheless, the local Lax-Friedrichs method is implemented here. Differently from the global Lax-Friedrichs method, in the local Lax-Friedrichs method, the $\max(\tilde{u}_A + a_A, \tilde{u}_B + a_B)$ is used instead of $\frac{\Delta x}{\Delta t}$. Furthermore, the local method is less dissipative then the global method.

3.4 NASA Chemical Equilibrium with Applications

The Chemical Equilibrium with Applications code [22], or CEA code, is a complex code and capable of making several analyses. This code reads a file input where is specified the problem case, it may be the rocket problem or the Champan-Jouguet detonation problem and so on. For the purpose of this work it was chosen the assigned internal energy and volume problem. Once specified the inputs, that are the internal energy, the volume mixture and the moles of the reactants, it gives as results the thermodynamic

variable and the mole fractions. The CEA code also offers the chance to choose the product species. It is good practice to select certain species, the significant ones, in order to simplify the complexity of the problem. The temperature and the pressure are the variables of interest, in this case, when the CFD code and the CEA code are linked. Because of the complexity of the CEA code, it was thought to develop a numerical code able to predict the equilibrium temperature of the mixture, making use of an iteration method, such as the Newton's method.

3.4.1 Iterative procedure and correction variables

Both the minimization of the Gibbs energy and the Helmhotz energy lead to a non-linear equations system. In order to solve it, the Newton-Raphson method is used. It is based on the Taylor series expansion of the functions, the terms with derivatives higher than one are truncated.

$$f_i\left(x_j^{k+1}\right) = f_i\left(x_j^{k}\right) + \frac{\partial f_i}{\partial x_j}\,\Delta x_j + O\left(\| \Delta x_j \|^2\right) \tag{3.23}$$

Imposing the left term of the equation 3.23 equal to zero leads to the following system:

$$f_i\left(x_j^{k+1}\right) = 0 \implies \begin{cases} \frac{\partial f_i}{\partial x_j}\,\Delta x_j = -f_i\left(x_j^{k}\right) \\ x_j^{k+1} = x_j^{k} + \Delta x_j \end{cases} \tag{3.24}$$

From the first equation of the system above the correction variable Δx_j is obtained and then is substituted in the second equation, as a consequence x_j^{k+1} is found. This process occurs iterative until the convergence is obtained. Furthermore, for the two methods explained in 2.2.1 and 2.2.2, it can be written the functions to use in the system 3.24.

$$x_j = \left\{\ln n_j\,, n_j, \ln n, \ln T\right\} \tag{3.25}$$

The variables involved in the two methods are expressed in 3.25 and the correction variables are the following:

$$\Delta x_j = \left\{\Delta\ln n_j\,, \Delta n_j, \Delta\ln n, \Delta\ln T\right\} \tag{3.26}$$

3.4.2 Iterative Gibbs equations

The equations involved in the minimization of the Gibbs energy can be expressed in five equations in order to apply the iterative method. These functions are:

$$f_1 = \mu_j + \sum_{i=1}^{l} \lambda_i a_{ij} \quad with \quad (j = 1, \dots, NS) \tag{3.27}$$

$$f_2 = \sum_{j=1}^{NS} a_{ij} n_j - b_i^{\circ} \quad with \quad (j = 1, \dots, NS) \tag{3.28}$$

$$f_3 = \sum_{j=1}^{NG} n_j - n \tag{3.29}$$

$$f_4 = h - h_o \tag{3.30}$$

$$f_5 = s - s_o \tag{3.31}$$

$$\frac{\partial f}{\partial \ln n_j} \Delta \ln n_j + \frac{\partial f}{\partial n_j} \Delta n_j + \frac{\partial f}{\partial \ln n} \Delta \ln n + \frac{\partial f}{\partial \ln T} \Delta \ln T = -f \tag{3.32}$$

In order to make dimensionless the functions above, they are divided by RT. By substituting every function from 3.27 to 3.31 in 3.32 and with the aid of equations 2.25, 2.26, 2.27 and 2.28 permits to find the following equations:

$$\Delta \ln n_j - \sum_{i=1}^{l} \pi_i a_{ij} - \Delta \ln n - \frac{H_j^{\circ}}{RT} \Delta \ln T = -\frac{\mu_j}{RT} \quad with \quad (j = 1, \dots., NG) \tag{3.33}$$

$$- \sum_{i=1}^{l} \pi_i a_{ij} - \frac{H_j^{\circ}}{RT} \Delta \ln T = -\frac{\mu_j}{RT} \quad with \quad (j = NG + 1, \dots., NS) \tag{3.34}$$

$$\sum_{j=1}^{NG} a_{kj} n_j \Delta \ln n_j + \sum_{j=NG+1}^{NS} a_{kj} \Delta n_j = b_k^{\circ} - b_k \ with \ (k = 1, \dots, l) \tag{3.35}$$

$$\sum_{j=1}^{NG} n_j \Delta \ln n_j - n\Delta \ln n = n - \sum_{j=1}^{NG} n_j \tag{3.36}$$

$$\sum_{j=1}^{NG} \frac{n_j H_j^{\circ}}{RT} \Delta \ln n_j + \sum_{j=NG+1}^{NS} \frac{H_j^{\circ}}{RT} \Delta n_j + \left(\sum_{j=1}^{NS} \frac{n_j C_{p,j}^{\circ}}{R} \right) \Delta \ln T = \frac{h_o - h}{RT} \tag{3.37}$$

$$\sum_{j=1}^{NG} \frac{n_j S_j^{\circ}}{R} \Delta \ln n_j + \sum_{j=NG+1}^{NS} \frac{S_j^{\circ}}{R} \Delta n_j + \left(\sum_{j=1}^{NS} \frac{n_j C_{p,j}^{\circ}}{R} \right) \Delta \ln T = \frac{s_o - s}{R} + n - \sum_{j=1}^{NG} n_j \quad (3.38)$$

When significant amount of species are considered in the problem, large numbers of simultaneous equations must be solved. So as to avoid that, the equations of the system can be reduced simply by substituting the expression for $\Delta \ln n_j$, by solving the equation 3.33, in the equations from 3.35 to 3.38. The resultant equations are shown in the following.

$$\sum_{i=1}^{l} \sum_{j=1}^{NG} a_{kj} a_{ij} n_j \pi_i + \sum_{j=NG+1}^{NS} a_{kj} \Delta n_j + \left(\sum_{j=1}^{NG} a_{kj} n_j \right) \Delta \ln n + \left(\sum_{j=1}^{NG} \frac{a_{kj} n_j H_j^{\circ}}{RT} \right) \Delta \ln T = b_k^{\circ} - b_k + \\ + \sum_{j=1}^{NG} \frac{a_{kj} n_j \mu_j}{RT} \quad with \quad (k = 1, \dots, l) \quad (3.39)$$

$$\sum_{i=1}^{l} \pi_i a_{ij} + \frac{H_j^{\circ}}{RT} \Delta \ln T = \frac{\mu_j}{RT} \quad with \quad (j = NG+1, \dots, NS) \quad (3.40)$$

$$\sum_{i=1}^{l} \sum_{j=1}^{NG} a_{ij} n_j \pi_i + \left(\sum_{j=1}^{NG} n_j - n \right) \Delta \ln n + \left(\sum_{j=1}^{NG} \frac{n_j H_j^{\circ}}{RT} \right) \Delta \ln T = n - \sum_{j=1}^{NG} n_j + \sum_{j=1}^{NG} \frac{n_j \mu_j}{RT} \quad (3.41)$$

$$\sum_{i=1}^{l} \left(\sum_{j=1}^{NG} \frac{a_{ij} n_j H_j^{\circ}}{RT} \right) \pi_i + \sum_{j=NG+1}^{NS} \frac{H_j^{\circ}}{RT} \Delta n_j + \left(\sum_{j=1}^{NG} \frac{n_j H_j^{\circ}}{RT} \right) \Delta \ln n + \left[\sum_{j=1}^{NS} \frac{n_j C_{p,j}^{\circ}}{R} + \sum_{j=1}^{NG} \frac{n_j \left(H_j^{\circ} \right)^2}{R^2 T^2} \right] \Delta \ln T = \frac{h_o - h}{RT} + \\ + \sum_{j=1}^{NG} \frac{n_j H_j^{\circ} \mu_j}{R^2 T^2} \quad (3.42)$$

$$\sum_{i=1}^{l} \left(\sum_{j=1}^{NG} \frac{a_{ij} n_j S_j^{\circ}}{R} \right) \pi_i + \sum_{j=NG+1}^{NS} \frac{S_j^{\circ}}{R} \Delta n_j + \left(\sum_{j=1}^{NG} \frac{n_j S_j^{\circ}}{R} \right) \Delta \ln n + \left[\sum_{j=1}^{NS} \frac{n_j C_{p,j}^{\circ}}{R} + \sum_{j=1}^{NG} \frac{n_j H_j^{\circ} S_j^{\circ}}{R^2 T} \right] \Delta \ln T = \frac{s_o - s}{RT} + n - \\ - \sum_{j=1}^{NG} n_j + \sum_{j=1}^{NG} \frac{n_j S_j^{\circ} \mu_j}{R^2 T} \quad (3.43)$$

3.4.3 Iterative Helmhotz equations

In the same way, the equations involved in the minimization of the Helmhotz energy are treated as the equations before. The difference is that the function 3.30 involves the specific internal energy and it is written below.

$$f_4 = e - e_o \quad (3.44)$$

Moreover, the chemical potential 2.38 has a different definition respect to 2.27 and the variable n does not appear explicitly. As a consequence the correction variable $\Delta \ln n$ does not appear in the equations below, so the equation 3.29 is not used here.

$$\Delta \ln n_j - \sum_{i=1}^{l} \pi_i a_{ij} - \frac{E_j^{\circ}}{RT} \Delta \ln T = -\frac{\mu_j}{RT} \quad with \quad (j = 1, \dots., NG) \tag{3.45}$$

$$- \sum_{i=1}^{l} \pi_i a_{ij} - \frac{E_j^{\circ}}{RT} \Delta \ln T = -\frac{\mu_j}{RT} \quad with \quad (j = NG + 1, \dots., NS) \tag{3.46}$$

$$\sum_{j=1}^{NG} a_{kj} n_j \Delta \ln n_j + \sum_{j=NG+1}^{NS} a_{kj} \Delta n_j = b_k^{\circ} - b_k \ with \ (k = 1, \dots, l) \tag{3.47}$$

$$\sum_{j=1}^{NG} \frac{n_j E_j^{\circ}}{RT} \Delta \ln n_j + \sum_{j=NG+1}^{NS} \frac{E_j^{\circ}}{RT} \Delta n_j + \left(\sum_{j=1}^{NS} \frac{n_j C_{v,j}^{\circ}}{R} \right) \Delta \ln T = \frac{u_o - u}{RT} \tag{3.48}$$

$$\sum_{j=1}^{NG} n_j \left(\frac{S_j}{R} - 1 \right) \Delta \ln n_j + \sum_{j=NG+1}^{NS} \frac{S_j}{R} \Delta n_j + \left(\sum_{j=1}^{NS} \frac{n_j C_{v,j}^{\circ}}{R} \right) \Delta \ln T = \frac{s_o - s}{R} \tag{3.49}$$

Even here it is necessary to reduce the equations of the system, in the same way this goal is reached by substituting the expression for $\Delta \ln n_j$, by solving 3.45, in the equations from 3.47 to 3.49.

$$\sum_{i=1}^{l} \sum_{j=1}^{NG} a_{kj} a_{ij} n_j \pi_i + \sum_{j=NG+1}^{NS} a_{kj} \Delta n_j + \left(\sum_{j=1}^{NG} \frac{a_{kj} n_j E_j^{\circ}}{RT} \right) \Delta \ln T = b_k^{\circ} - b_k + \sum_{j=1}^{NG} \frac{a_{kj} n_j \mu_j}{RT}$$
$$with \quad (k = 1, \dots., l) \tag{3.50}$$

$$\sum_{i=1}^{l} \pi_i a_{ij} + \frac{E_j^{\circ}}{RT} \Delta \ln T = \frac{\mu_j}{RT} \quad with \quad (j = NG + 1, \dots., NS) \tag{3.51}$$

$$\sum_{i=1}^{l} \left(\sum_{j=1}^{NG} \frac{a_{ij} n_j E_j^{\circ}}{RT} \right) \pi_i + \sum_{j=NG+1}^{NS} \frac{E_j^{\circ}}{RT} \Delta n_j + \left[\sum_{j=1}^{NS} \frac{n_j C_{v,j}^{\circ}}{R} + \sum_{j=1}^{NG} \frac{n_j \left(E_j^{\circ} \right)^2}{R^2 T^2} \right] \Delta \ln T = \frac{e_o - e}{RT} + + \sum_{j=1}^{NG} \frac{n_j E_j^{\circ} \mu_j}{R^2 T^2} \tag{3.52}$$

$$\sum_{i=1}^{l} \left(\sum_{j=1}^{NG} \frac{a_{ij} n_j (S_j - R)}{R} \right) \pi_i + \sum_{j=NG+1}^{NS} \frac{S_j}{R} \Delta n_j + \left[\sum_{j=1}^{NS} \frac{n_j C_{v,j}^{\circ}}{R} + \sum_{j=1}^{NG} \frac{n_j E_j^{\circ} (S_j - R)}{R^2 T} \right] \Delta \ln T = \frac{s_o - s}{RT} + \sum_{j=1}^{NG} \frac{n_j (S_j - R) \mu_j}{R^2 T} \tag{3.53}$$

Once the two thermodynamic state variables are chosen, the equations of the system can be solved and the correction variables are found and then the process is repeated until

convergence. Therefore, it is needed to set initial estimates of those variables and rights criteria of convergence have to be applied.

3.4.4 Initial estimates and convergence for obtaining equilibrium compositions

A simple procedure is used to set the initial estimates in [16], also the optimal convergence criteria are used in [16] and they are explained in this paragraph.

For the first iteration of the first point is assigned $n = 0.1$, in other words the molecular weight is assigned to 10 kg/mole. The number of moles of each species per kilogram of mixture is set $0.1/NG$, where NG is the number of gaseous species. Furthermore, if the temperature is not assigned as input variables, the initial estimate for the temperature is $T = 3800\,K$. After the first step the results are used as new initial estimates. This technique for the initial conditions provides poor initial estimate, nevertheless this simple procedure is preferable for general chemistry problem. As a consequence, given these initial estimates, it is needed to choose the convergence criteria.

There are two situations when the iteration equations give large corrections. The first situation is at the beginning of the iteration and it is due to the poor estimates, when there a small amount of species the other situation occurs, because of the iteration procedure attempts to increase the moles of that species. In order to handle these problems, a control factor λ_c is used; this permits to avoid the large increase of $\ln n_j$ $(j = 1, \dots., NG)$, n_j $(j = NG + 1, \dots., NS)$, $\ln n$ and $\ln T$. The corrections for temperature T and n are limited to $e^{0.4}$, moreover for the gaseous species are implemented two definitions for λ_c and they are based on the control parameter SIZE. The parameter SIZE is included to save the computation time; this is done by calculating n_j only for those species with moles fractions greater than the parameter SIZE that is imposed as SIZE $= 18.420681$. If $\ln \frac{n_j}{n} \geq -\text{SIZE}$ then the correction for n_j is limited to e^2 and the control factor is calculated as:

$$\lambda_{1c} = \frac{2}{\max\left(5|\Delta \ln T|, 5|\Delta \ln n|, |\Delta \ln n_j|\right)} \tag{3.54}$$

In the event that $\ln\frac{n_j}{n} < -\text{SIZE}$ and $\Delta \ln n_j \geq 0$, the control factor is:

$$\lambda_{2c} = \min \left| \frac{-\ln\frac{n_j}{n} - 9.2103404}{\Delta \ln n_j - \Delta \ln n} \right| \tag{3.55}$$

The control factor λ_c that appears in the equation below is chosen as the minimum between 1, λ_{1c} and λ_{2c}.

$$\ln n_j^{i+1} = \ln n_j^i + \lambda_c^i \Delta \ln n_j^i \;\; with \;\; (j = 1, \ldots., NG) \tag{3.56}$$

$$n_j^{i+1} = n_j^i + \lambda_c^i \Delta n_j^i \;\; with \;\; (j = NG + 1, \ldots., NS) \tag{3.57}$$

$$\ln n^{i+1} = \ln n^i + \lambda_c^i \Delta \ln n^i \tag{3.58}$$

$$\ln T^{i+1} = \ln T^i + \lambda_c^i \Delta \ln T^i \tag{3.59}$$

In the equations above the superscript *i* refers to the *i*-th estimate. When the values of the estimates are close to the equilibrium values λ_c will be equal to one, otherwise it will be less than one. The correction variables have to respect certain criteria until the convergence; these are shown in the following.

$$\frac{n_j |\Delta \ln n_j|}{\sum_{j=1}^{NS} n_j} \leq 0.5\times10^{-5} \; with \;\; (j = 1, \ldots., NG) \tag{3.60}$$

$$\frac{|\Delta n_j|}{\sum_{j=1}^{NS} n_j} \leq 0.5\times10^{-5} \;\; with \;\; (j = NG + 1, \ldots., NS) \tag{3.61}$$

$$\frac{n|\Delta \ln n|}{\sum_{j=1}^{NS} n_j} \leq 0.5\times10^{-5} \tag{3.62}$$

The temperature is shown as a variable in the problem case of this thesis and it is needed a criteria for the convergence, this is shown below.

$$\Delta \ln T \leq 1.0\times10^{-4} \tag{3.63}$$

Furthermore, the convergence test for those species with $b_0^i \geq 1.0\times10^{-6}$ is:

$$\left|b_o^i - \sum_{j=1}^{NS} n_j a_{ij}\right| \leq \left(b_0^i\right)_{max} \times 1.0\times10^{-4} \;\; with \;\; (i = 1,..,l) \tag{3.64}$$

Others criteria are imposed for those problems where the entropy is assigned and when the parameter TRACE is not equal to zero. For the first one is imposed the following condition:

$$\left|\frac{S_o - S}{R}\right| \leq 0.5\times10^{-4} \tag{3.65}$$

While for the second one is imposed a condition for the variable $\pi_i = \frac{\lambda_i}{RT}$ and it is expressed as:

$$\left|\frac{\pi_i^k - \pi_i^{k+1}}{\pi_i^{k+1}}\right| \leq 0.001 \quad with \quad (i = 1, \ldots l) \tag{3.66}$$

The parameter TRACE is an input parameter and its default value is zero. The aim of this parameter is the choice of the value for SIZE, for the value of ITN (the maximum iteration number) and for the values of the other practical parameters that are required for the different species. Nevertheless there is also a test for the condensed species in order to include or not to include them. This test is done with the aid of the Gibbs energy; if the condensed species are present in the mixture, the variation of the Gibbs energy respect to n_j is lower than zero.

$$\frac{\partial G}{\partial n_j} = \left(\frac{\mu_j^o}{RT}\right)_c - \sum_{i=1}^{l} \pi_i a_{ij} < 0 \tag{3.67}$$

The subscript *c* refers to the condensed species. Furthermore, the equation 3.67 can be used even if the gas phase of the species corresponding to the condensed species is not present. The species, whose respect the equation 3.67, are included in the mixture, and when several condensed species are present only the species with larger negative value of $\frac{\partial G}{\partial n_j}$ are considered. After the equilibrium composition is reached, if the concentrations

of the condensed species are negative, they are removed and a new equilibrium composition is obtained.

3.5 Newton's method for the equilibrium temperature

Although the optimal results provided from the CEA code, its complexity involves a substantial computational code. The aim of this additional code is to reduce this computational cost and the goal is to minimize calls to the CEA code. This code is less complex than the CEA code, but it requires some results provided by CEA code as inputs. These results are the mole fractions of the product species; in addition also the internal energy and the density of the mixture is required. Every chemical species together with their properties are stored into a library file. For each species, the specific enthalpy, the specific heat at constant pressure and the specific entropy are functions of the temperature and they have the following forms.

$$\frac{H^\circ}{RT} = \frac{\int C_p^\circ dT}{RT} \tag{3.68}$$

$$\frac{C_p{}^\circ}{R} = \sum_i a_i T^{q_i} \tag{3.69}$$

$$\frac{S^\circ}{R} = \int \frac{C_p^\circ dT}{RT} \tag{3.70}$$

The equations 3.68, 3.69 and 3.70 are the general forms, while in the chemical equilibrium program is used a fourth order polynomial form [16].

$$\frac{C_p{}^\circ}{R} = a_1 T^{-2} + a_2 T^{-1} + a_3 + a_4 T + a_5 T^2 + a_6 T^3 + a_7 T^4 \tag{3.71}$$

$$\frac{H^\circ}{RT} = -a_1 T^{-2} + a_2 T^{-1} \ln T + a_3 + a_4 \frac{T}{2} + a_5 \frac{T^2}{3} + a_6 \frac{T^3}{4} + a_7 \frac{T^4}{5} + \frac{a_8}{T} \tag{3.72}$$

$$\frac{S^\circ}{R} = -a_1 \frac{T^{-2}}{2} - a_2 T^{-1} + a_3 \ln T + a_4 T + a_5 \frac{T^2}{2} + a_6 \frac{T^3}{3} + a_7 \frac{T^4}{4} + a_9 \tag{3.73}$$

The equation 3.71 and 3.72 are implemented in the iterative loop but they are multiplied with X_i, in other words the mole fractions of every species.

In those functions, the constant coefficients a_i are stored into the library file early mentioned and they are different for each species. Furthermore, there are three sets of constant coefficients and which one to choose depends on the thermal range. The three intervals are 200 to 1000 K, 1000 to 6000 K and 6000 to 20000 K. During the iterative procedure, the additional code is able to read from the library file the constant coefficients based on the right temperature range.
The iterative procedure is based on the classic Newton's method.

$$T_{k+1} = T_k - \frac{f(T_k)}{f'(T_k)} \tag{3.74}$$

In the equation 3.74, the function $f(T_k)$ and its derivate $f'(T_k)$ have the following forms:

$$f(T_k) = \frac{e}{R} - \frac{H^\circ}{R} + \frac{T_k}{PM} \tag{3.75}$$

$$f'(T_k) = -\frac{C_p^\circ}{R} + \frac{1}{PM} \tag{3.76}$$

The variable PM is the molecular weight of the mixture and is related to the molecular weight of every species PM_i, therefore the definition for PM is the following:

$$PM = \sum_{i=1}^{NS} X_i PM_i \tag{3.77}$$

The code is able to read the right coefficients of the species that are considered in the simulation. Then the equation 3.75 and 3.76 are initialized with $T = 3800\ K$, after that a while loop starts as long as the condition is respected, in other words it continues as long as *ERR_T>TOL_T*. The variable *ERR_T* is defined as:

$$ERR\_T = \frac{abs(T - T_0)}{abs(T)} \tag{3.78}$$

In the equation 3.78, T_0 is the temperature at the earlier iteration and T is the temperature at the current iteration. The variable *TOL_T* is imposed as *TOL_T=1D-10.*

Furthermore on every iteration, there is also a control on the temperature, so as to check in which of the three temperature intervals fall and so which coefficients have to be chosen.
Once the while loop ends the temperature is found and also the pressure, this last one is calculated from the gas equation as following:

$$p = \rho \tilde{R} T \tag{3.79}$$

In the equation above $\tilde{R}$ is the specific gas constant of the mixture and its dimension is $\left[\frac{kJ}{kgK}\right]$, while R, in the previous equations, is the gas constant and its value is $R = 8.314\ \left[\frac{J}{molK}\right]$.

3.6 Finite volume method for the one-dimensional thermal model

For the discretization of the one-dimensional heat conduction equation is used the finite volume method, as in the quasi-one-dimensional gas-dynamic model.
The equation 2.44 is in the form of the convective-diffusion equation. The diffusion term is the conductive term that comes directly from the heat equation, while the convective term, or better the advection term, comes out because the equation is written in a reference system located in the solid-fuel regression surface.
The solid-fuel domain is discretized as it was done from the gas-dynamic model, but with the difference that the nodes grid are not uniformly spaced. This difference will be better explained in the paragraph 4.4.
Each terms of the equation 2.44 are integrated on an arbitrary volume and then the average value at the centre of the cell is taken.

$$\frac{\partial}{\partial t}\int_{y_{i-\frac{1}{2}}}^{y_{i+\frac{1}{2}}} T dy = \int_{y_{i-\frac{1}{2}}}^{y_{i+\frac{1}{2}}} \dot{r}\frac{\partial T}{\partial y} dy + \int_{y_{i-\frac{1}{2}}}^{y_{i+\frac{1}{2}}} \alpha \frac{\partial^2 T}{\partial y^2} dy \tag{3.80}$$

$$T_i = \frac{1}{\Delta y}\int_{y_{i-\frac{1}{2}}}^{y_{i+\frac{1}{2}}} T dy \tag{3.81}$$

By developing the calculations, the following expression is found.

$$\frac{\partial T_i}{\partial t} = \dot{r}\,\frac{T_{i+\frac{1}{2}} - T_{i-\frac{1}{2}}}{\Delta y} + \alpha\,\frac{\left(\frac{\partial T}{\partial y}\right)_{i+\frac{1}{2}} - \left(\frac{\partial T}{\partial y}\right)_{i-\frac{1}{2}}}{\Delta y} \tag{3.82}$$

Differently from the choice that it is done for the gas dynamic fluxes, here it is chosen to apply the forward scheme for the first term in the right hand. As a consequence it can be written $T_{i+1} = T_{i+\frac{1}{2}}$ and $T_i = T_{i-\frac{1}{2}}$, so this is an "Upwind" scheme. For the second term on the right hand, instead, it is chosen to apply the central scheme.

$$\frac{\partial T_i}{\partial t} = \dot{r}\,\frac{T_{i+1} - T_i}{\Delta y} + \alpha\,\frac{T_{i+1} - 2T_i + T_{i-1}}{\Delta y^2} \tag{3.83}$$

For the time integration the explicit Euler is implemented, as a consequence the accuracy of the system is of the first order.

$$T_i^{n+1} = T_i^n + \frac{\partial T_i}{\partial t}\Delta t \tag{3.84}$$

The equation 2.48 has to be implemented in order to close the problem. As it can be seen from that equation, the regression rate is function of the wall-temperature, thus, this temperature is solved iteratively using the bisection method.
For the bisection method the function implemented is the following:

$$FNR = \dot{Q}_w + \frac{k(T_1 - T_w)}{\Delta y} - \rho_f L_v A_h e^{-\frac{E_a}{RT_w}} \tag{3.85}$$

In the equation 3.85 appears the wall-heat flux $\dot{Q}_w$ and as it is seen in the paragraph 2.3.1, there are two expression based on the blowing parameter. The wall-heat flux expressions are rewritten so as to be function of the oxidizer mass flux; these new expressions are shown in the following.

$$\dot{Q}_w = A_1 G_{ox}^n - A_2\dot{r} \qquad if\ B \le B^* \tag{3.86}$$

$$\dot{Q}_w = A_3 G_{ox}^{\frac{n}{1-k}}\dot{r}^{-\frac{k}{1-k}} \qquad if\ B > B^* \tag{3.87}$$

Where $n = 0.8$ and the other coefficients are valuated as the following.

$$A_1 = \frac{1}{2} C_{f0ref} G_{oxref}^{1-n} \; B_{ref} h_{vref} \tag{3.88}$$

$$A_2 = 0.4 \rho_f B_{ref} h_{vref} \tag{3.89}$$

$$A_3 = \frac{\dot{Q}_{wref}}{\left(G_{oxref}^{n} \dot{r}_{ref}^{-k}\right)^{\frac{1}{1-k}}} \tag{3.90}$$

For the coefficients A_1 and A_2 it is supposed that the blowing parameter is equal to the thermochemical blowing parameter in the steady state condition.

According to the study of M. Arif Karabeyoglu [14], in this code it was also implemented another subroutine so as to take into consideration the boundary layer time delay τ_{BL}. In that subroutine, the regression rate is solved at the time $t - \tau_{BL}$. The relations for the wall-heat flux are modified consequently.

$$\dot{Q}_w = A_1 G_{ox}^{n} - A_2 \dot{r}(t - \tau_{BL}) \qquad if \; B \leq B^* \tag{3.91}$$

$$\dot{Q}_w = A_3 G_{ox}^{\frac{n}{1-k}} \dot{r}(t - \tau_{BL})^{-\frac{k}{1-k}} \qquad if \; B > B^* \tag{3.92}$$

Chapter 4

Numerical Results

4.1 Comparing results between CEA code and TEST code

Once the three numerical models are completed, before linking them together, they have to be tested and validated. It was seen that once the CFD code and the CEA code are linked, the long computational time occurs, thus, it is needed to find out that problem. The long computational time was due to the CEA code complexity and therefore it has to be run at every point along the combustion chamber. As it was explained in the paragraph 3.4 of the chapter 3, its complexity is due to the several problems it is able to solve and on the reading and writing procedure from file. As a consequence, it was thought to develop a numerical code simpler than the CEA code but that it is able to give the same results of the CEA. The goal is to reduce the calls to the chemical code at every time step. The TEST code takes the mole fractions of the product species, internal energy and density of the mixture as inputs and it gives temperature and pressure as outputs. Obviously several tests were made before using this code together with the other two. In order to validate the code, some chemical species mixture were chosen and then the results were compared with the CEA code. In the tables below are exposed some results, the specific internal energy and the density are the same for each of the exposed chemical reactions $\left(e_i = 1.6920e + 03 \left[\frac{kJ}{kg}\right], \rho = 0.88625 \left[\frac{kg}{m^3}\right]\right)$.

Reactants	$\boldsymbol{O_2 + H_2}$	
Products	$\boldsymbol{H + H_2 + H_2O + O + O_2}$	
	TEST code	**CEA code**
Temperature [K]	**2684.006**	**2684.01**
Pressure [BAR]	**6.4037**	**6.404**

Table 4.1. Temperature and pressure comparison between the two codes in the chemical reaction of O_2 and H_2

Reactants	$O_2 + N_2$	
Products	$N + N_2, +NO + O + O_2$	
	TEST code	CEA code
Temperature [K]	2331.64	2331.64
Pressure [BAR]	5.4178	5.4182

Table 4.2. Temperature and pressure comparison between the two codes in the chemical reaction of O_2 and N_2

Reactants	$O_2 + C_2H_4$	
Products	$C_2O + C_2H_4 + H + H_2 + H_2O + O + OH + O_2$	
	TEST code	CEA code
Temperature [K]	3319.217	3319.23
Pressure [BAR]	8.2664	8.2670

Table 4.3. Temperature and pressure comparison between the two codes in the chemical reaction of O_2 and C_2H_4

It is noted, from the tables above, that the temperature and the pressure provided by the TEST code are in good agreement with those of the CEA code.

4.2 Validation of coupled code results in a specific nozzle configuration

Thanks to the good results provided, once the TEST code is validated, it is linked together with the CFD code and the CEA code. Therefore, the TEST code runs at every time step; it takes the mole fractions from the CEA, the specific internal energy and the density from the CFD code as inputs and gives the temperature and the pressure as outputs. As it did for the TEST code also for these coupled codes, the results have to be validated. In order to do that, it is thought to compare the mole fractions with those obtained from [23], where they are shown as function of the nozzle area ratio. It was chosen a nozzle geometry in which the area ratio is variable from one to ten $\rightarrow \frac{A}{A^*} = [1: 10]$; A is the generic nozzle area while A^* is the throttle area. The chemical species are those exposed in the table 4.2; the total temperature and total pressure of the mixture are the following: $T_o = 8000\ [K]$; $P_o = 100\ [atm]$.

In the initial conditions the specific internal energy can not be calculated with the following formula:

$$e_i = \frac{\tilde{R}T}{\gamma - 1} \tag{4.1}$$

The reason is that the specific gas constant $\tilde{R}$ and γ depend on the mixture composition. So as to calculate the specific internal energy, it is thought to run the CEA code by imposing the temperature and pressure instead of the specific internal energy and density. In addition, the code provides also the mole fractions and the ratio of the specific heats γ, then these are used to impose the boundary conditions at the inlet. The flow at the inlet is subsonic, thus, the boundary conditions have to be imposed by taking into consideration the signal that goes back from the inside of the domain. This can be done by using the method of characteristics and by imposing the total pressure, total temperature and the value of the Riemann invariant that goes back from the inside. Nevertheless, the expressions used for the signals are written for the ideal gases, in which the enthalpy and the internal energy are zero for $T = 0\ [K]$. Instead, in the CEA code, the internal energy and the enthalpy are expressed in a polynomial fitting as it can be seen in equation 3.72. In order to make coherent the values evaluated from the boundary conditions with the values evaluated from the CEA code, the *"bias"* is calculated between the two definitions of the internal energy.

$$bias = \rho e_i - \frac{p}{\gamma - 1} \tag{4.2}$$

Once this parameter is known and after the resolution of the boundary condition at the inlet pressure, temperature and density are known. As a consequence, the value of the specific internal energy multiplied by density is valuated as $\frac{p}{\gamma - 1}$ with the addition of the "$bias$".

It is worth noting that for the outlet no boundary conditions have to be imposed because of the supersonic nature of the flow, that simplify the work and for all the simulations the divergence part of the nozzle is considered.

Another important aspect to be highlighted concerns the evaluation of the fluxes to the interface through Lax-Friedrichs method; differently from the classical method, because of the chemistry, the speed of sound in the neighbours cells has to be calculated by knowing the temperature and also the ratio of the specific heats and the gas constant of the two adjacent cells.

The results are shown in the following.

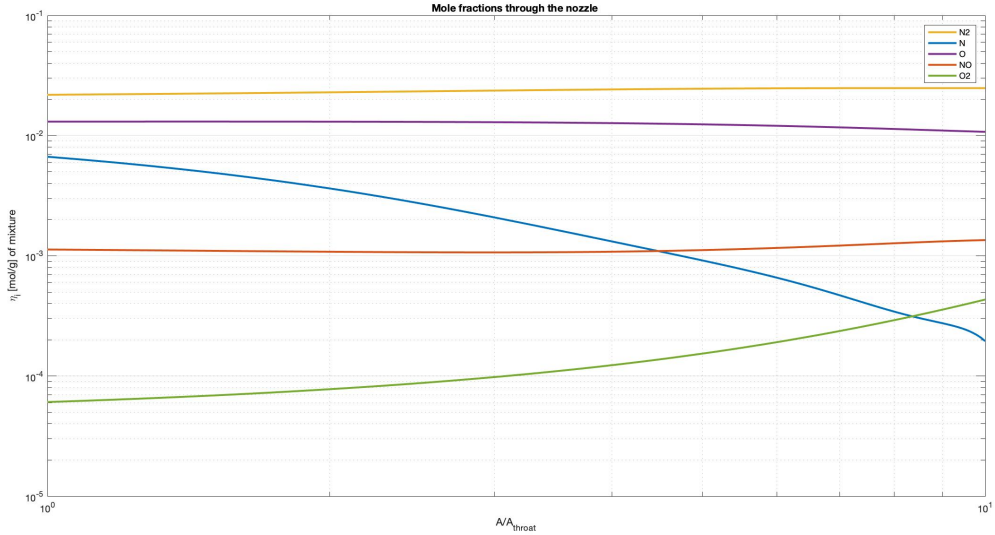

Figure 4.1. Mole fractions through the nozzle in [23]

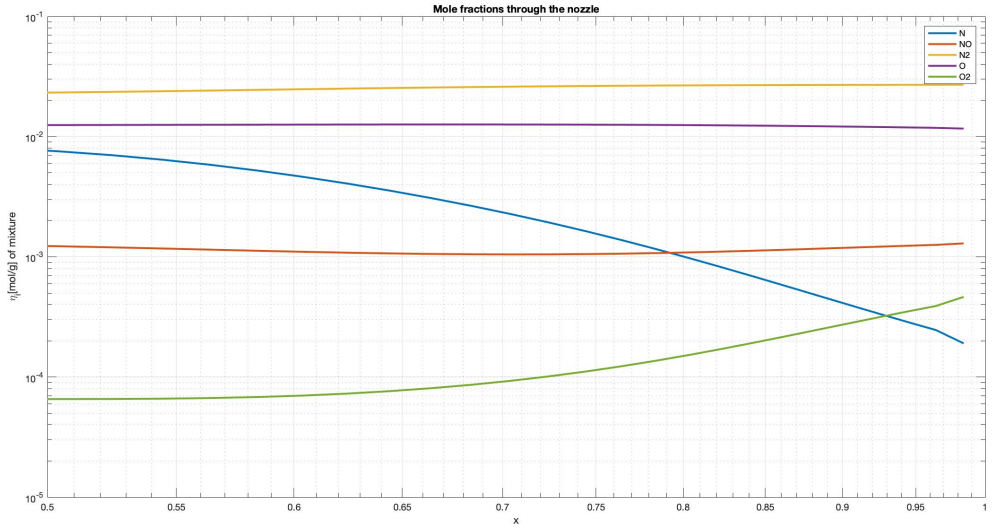

Figure 4.2. Mole fractions through the nozzle evaluated from the code

In figure 4.2 the divergence part of the nozzle starts from $x = 0.5$ to $x = 1$. The results are in good agreement with those exposed in figure 4.1. This is the proof that the three codes are successfully coupled.

4.3 Fluid dynamic flow-field in axial-injected hybrid rocket motor without thermal model

In the simulation exposed in the paragraph 4.2, there is not the source term and only the nozzle is considered. The code runs successfully, thus, the combustion chamber can be added at the nozzle geometry and also the source term, relative to the fuel mass addition, can be implemented. The new geometry is schematized in the figure below while the geometry parameters are exposed in the table 4.4.

Geometry data	
Port area	$\mathbf{4.13 * 10^{-4}\ [m^2]}$
Throat area	$\mathbf{2.065 * 10^{-4}\ [m^2]}$
Total Length	$\mathbf{1.09\ [m]}$
Chamber Length	$\mathbf{0.545\ [m]}$

Table 4.4. Geometry data of the Hybrid Rocket Engine

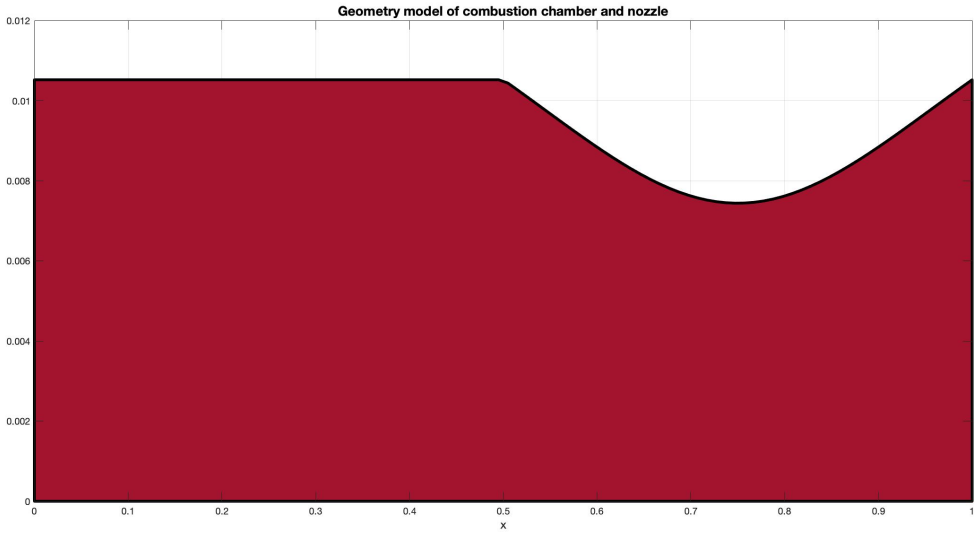

Figure 4.3. Schematic semi-geometry of the combustor and the nozzle of the Hybrid Rocket engine

The figure above shows the semi-geometry of the combustion chamber and nozzle of the hybrid rocket engine. Exactly the solid fuel is not schematized in that figure, only the geometry of the port area is shown; furthermore, the axis are normalized respect to the reference length, which is the total length of the rocket engine.

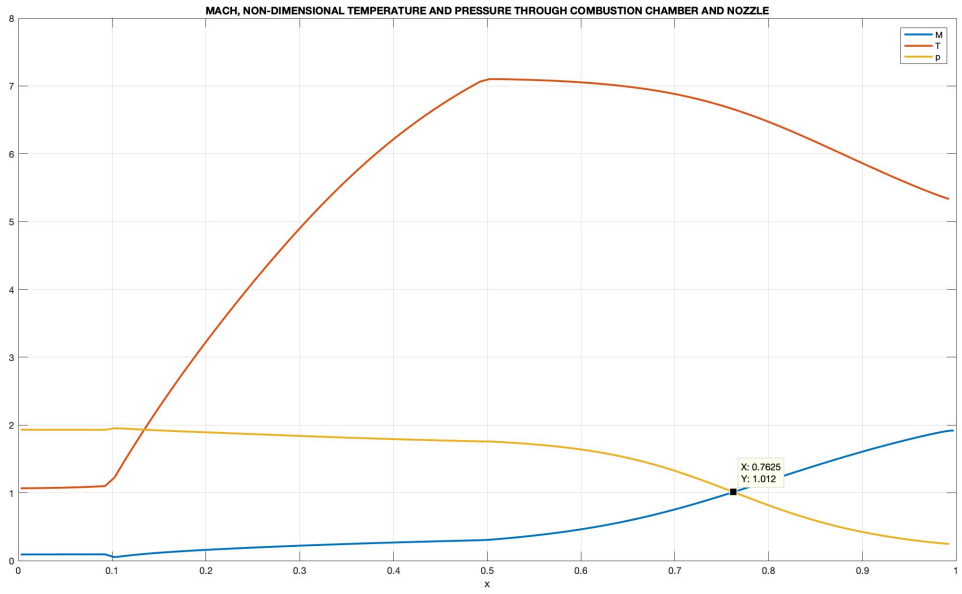

Figure 4.4. Fluid-dynamic flow field through the combustion chamber and the nozzle

The figure 4.4 represents the results of the fluid-dynamic flow-field through the combustion chamber and the nozzle of the hybrid rocket motor. In detail, it can be seen the Mach number, the non-dimensional temperature and the pressure in steady conditions.

The reference parameters used for the normalization of the equations and the results are exposed in the table below.

Reference parameters	
$\boldsymbol{T_{ref}}$	$\boldsymbol{300\ [K]}$
$\boldsymbol{P_{ref}}$	$\boldsymbol{9.553 * 10^5\ [Pa]}$
$\boldsymbol{\widetilde{R}_{ref}}$	$\boldsymbol{259.82\ \left[\frac{J}{kgK}\right]}$
$\boldsymbol{L_{ref}}$	$\boldsymbol{1.09\ [m]}$

Table 4.5. Reference parameters for the CFD code

Differently from the case exposed in paragraph 4.2, here the boundary conditions are not valuated with the Riemann invariants. In this case, the mass flow rate and the temperature of the oxidizer is imposed, the pressure is calculated from the internal flow field, then the density and the flow velocity are consequently obtained. Because of the presence of the fourth equation, the mixture fraction has to be initialized and it is set equal to 10^{-6}. This last value is not exactly zero because the CEA code does not run if the mole of the fuel is equal to zero.
Those boundary conditions for subsonic inlet are shown in the table 4.6.

Parameter	***Value given***
Pressure p	***Zeroth-order extrapolation from internal flow-field***
Temperature T	$\mathbf{300}\ [\boldsymbol{K}]$
Mass flow rate $\dot{m}_{ox}$	$\mathbf{0.14}\ \left[\boldsymbol{kg}/\boldsymbol{s}\right]$
Mixture fraction ϵ	$\mathbf{10^{-6}}$

Table 4.6. Boundary conditions for the CFD code

In this preliminary analysis, it is imposed a constant regression rate and so the fuel mass flow is constant during time $\left(\dot{r} = 0.0005\ \left[\frac{m}{s}\right], \dot{m}_f = 0.4795\ \left[\frac{kg}{m^2 s}\right]\right)$, the injection point of the fuel is for $x = 0.1$. In the same graph, it can be noted the end of a combustion chamber for $x = 0.5$, in other words the point where the temperature reaches its biggest value. Furthermore it is shown the nozzle throat area for $x \cong 0.76$.

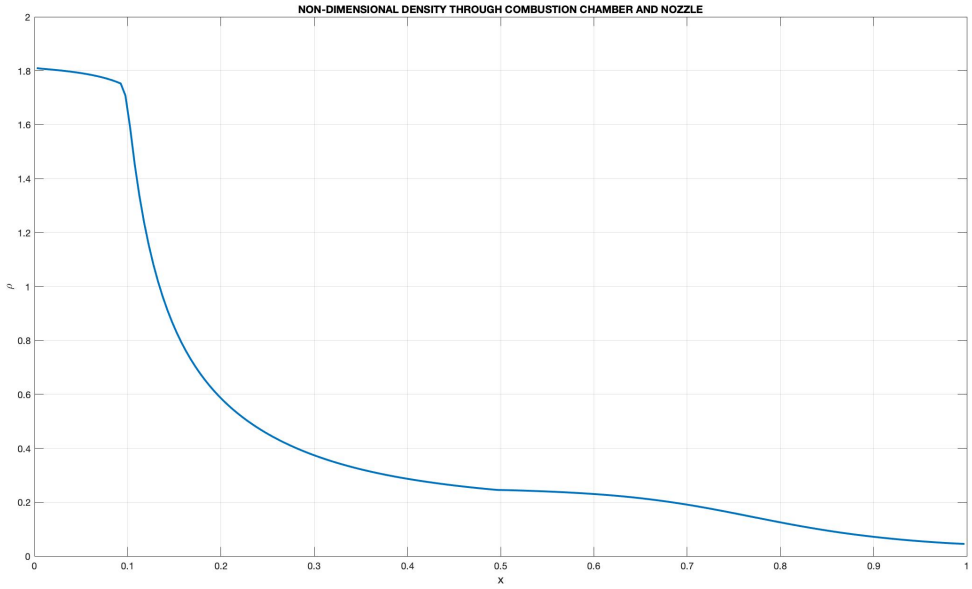

Figure 4.5. Density through the combustion chamber and the nozzle

The graph above represents the non-dimensional density in order to complete the physical quantities needed for the description of the fluid dynamic flow-field.

The figure 4.6 shows the mixture fraction ϵ through the hybrid rocket motor.

The graph provides a proof that the condition we are seeing is the steady condition, in fact the mixture ratio has a linear trend from $x = 0.1$ to $x = 0.5$, in other words the point of the fuel injection and the end of combustion chamber. Before and after those points, the mixture fraction assumes a constant shape.

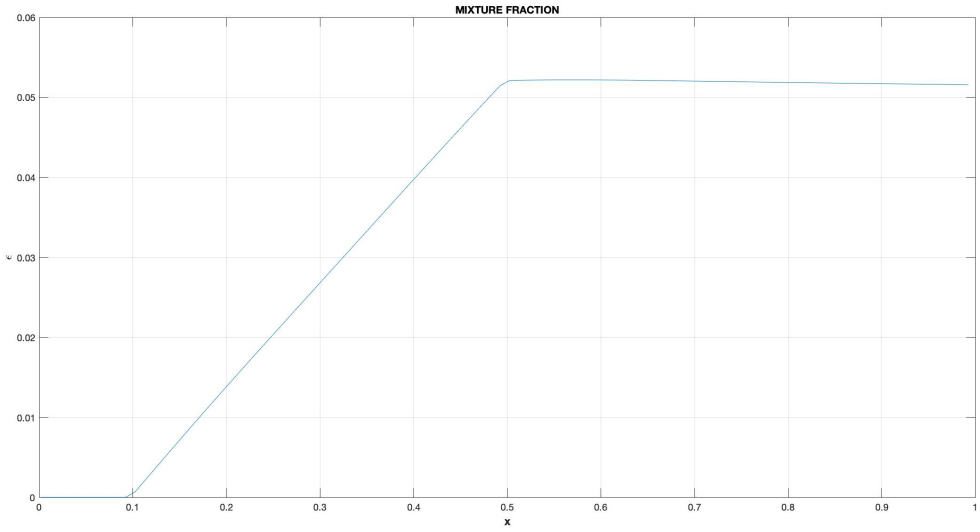

Figure 4.6. Mixture fraction through the combustion chamber and the nozzle

The mixture fraction ϵ provides the inputs for the CEA code in terms of reactant moles. Indeed, directly from its own definition, the mole number of Carbon element per unit mass of the mixture b_c is found, then with the following relations the moles of both reactants can be found.

$$b_{C_2H_4} = \frac{b_C}{2} \tag{4.3}$$

$$kg_{C_2H_4} = b_{C_2H_4} * Pm_{C_2H_4} \tag{4.4}$$

$$kg_{O_2} = 1 - kg_{C_2H_4} \tag{4.5}$$

$$b_{O_2} = \frac{kg_{O_2}}{Pm_{O_2}} \tag{4.6}$$

In these relation, $kg_{C_2H_4}$ and kg_{O_2} mean the kilogram of ethylene and oxygen in the actual mixture, while $Pm_{C_2H_4}$ and Pm_{O_2} are the molecular weight of both species express in $\left[\frac{kg}{mol}\right]$.

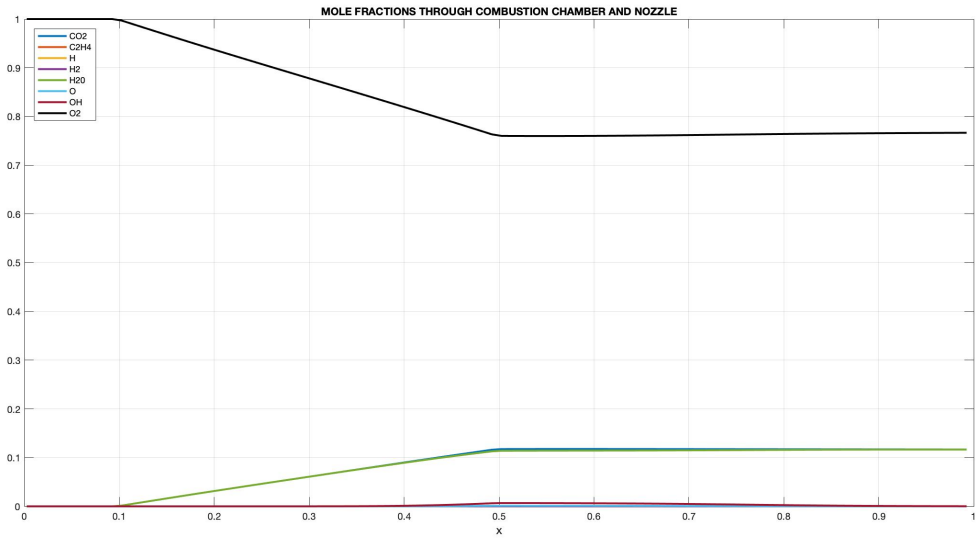

Figure 4.7. Mole fractions through the combustion chamber and the nozzle

As a conclusion, it is shown, in the figure 4.7, the mole fractions through the combustion chamber and the nozzle, and as we can expected the mole fraction of molecular oxygen decreases from $x = 0.1$ to $x = 0.5$, while the mole fractions of CO_2 and H_2O increase as a proof that the reaction with C_2H_4 is happening.

4.4 Fluid dynamic flow-field in axial-injected hybrid rocket motor with thermal model and without boundary layer delay time

In the previous simulation the regression rate is assumed to be constant and equal to $\dot{r} = 5d - 4\ \left[\frac{m}{s}\right]$. So as to find the right value of the regression rate the thermal code has to be implemented, because this parameter depends on the fuel grain surface temperature. In order to link this code with the others, the thermal properties of the solid-fuel are needed, in this case the solid-fuel is the HDPE.

The thermal properties are exposed in the table below and they have been taken from [24].

Thermal properties of HDPE	
Specific heat at constant pressure c_p	$\mathbf{3000}\left[\frac{\boldsymbol{J}}{\boldsymbol{kgK}}\right]$
Solid-fuel density ρ_f	$\mathbf{959}\left[\frac{\boldsymbol{kg}}{\boldsymbol{m^3}}\right]$
Heat of vaporization L_v	$\mathbf{22 * 10^5}\left[\frac{\boldsymbol{J}}{\boldsymbol{kg}}\right]$
Activation energy E_a	$\mathbf{63}\left[\frac{\boldsymbol{kcal}}{\boldsymbol{mol}}\right]$
Thermal diffusivity α	$\mathbf{1.3208 * 10^{-7}}\left[\frac{\boldsymbol{m^2}}{\boldsymbol{s}}\right]$

Table 4.7. Thermo-physical properties of HDPE

The domain of the solid-fuel is set $[0,100\delta]$ where $\delta = \alpha/\dot{r}_{ref}$, therefore the number of spatial point in this domain is $N = 40$. Because of the largest gradients in the temperature occur near the regression surface, the grid nodes are spaced non-uniformly; the first node is placed at 0.005 $[mm]$ while the distance between the other adjacent nodes increase by 11.5% towards the outside of the fuel-grain. The grid nodes along the combustor and nozzle are instead equal to 100 and they are uniformly spaced.

The reference parameters for the thermal code are exposed in the table below.

Reference parameters	
$T_{w_{ref}}$	$622.5\ [K]$
$\dot{r}_{ref}$	$0.541 * 10^{-3}\ \left[\frac{m}{s}\right]$
B_{ref}	5.313
L_{ref}	$0.545\ [m]$
$G_{ox_{ref}}$	$100\ \left[\frac{kg}{m^2 s}\right]$
$C_{f0_{ref}}$	$6.47 * 10^{-3}$

Table 4.8. Reference parameters for the thermal code

The results of that simulation are exposed in the figure below.

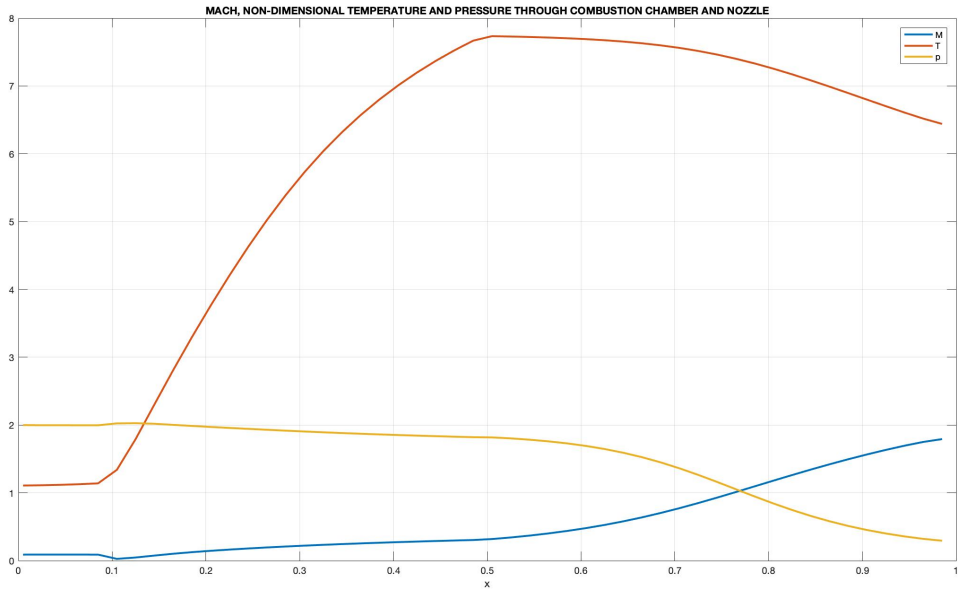

Figure 4.8. Fluid-dynamic flow field through the combustion chamber and the nozzle by adding the thermal model

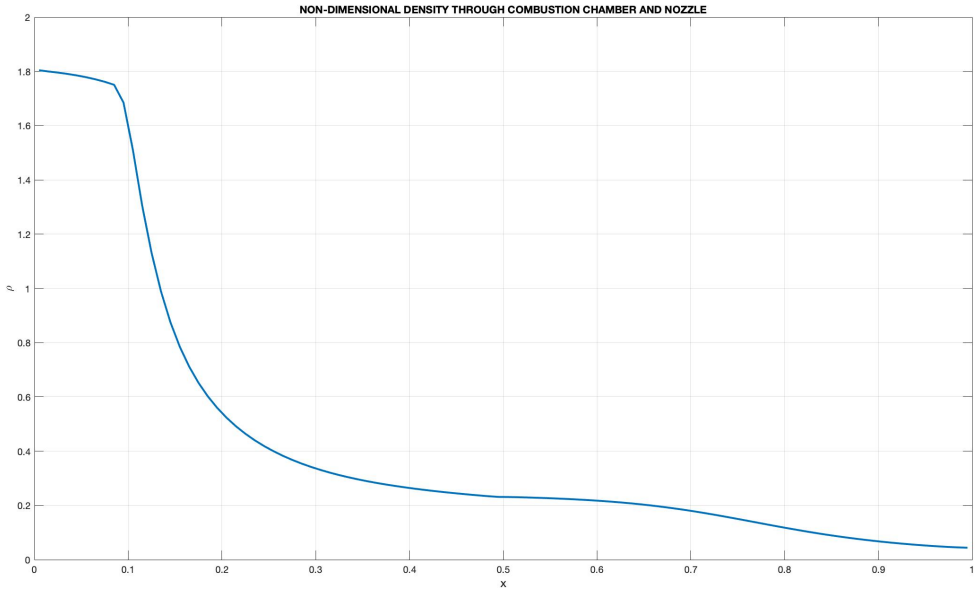

Figure 4.9. Density through the combustion chamber and the nozzle by adding the thermal model

The fluid-dynamic flow-field is not so much different from the previous simulation. This happens because the value of the regression rate found with the aid of the thermal code is not really different from the previous value. Obviously, now the value of the regression rate is correctly found according to the solid fuel surface temperature; the code is able to take into consideration the effects of some parameters such as the blowing parameter, the activation energy and the boundary delay time, which are the fundamental parameters responsible for the instability phenomena according to [14].

Even if the value of the regression rate differs slightly from the previous value, it is worth noting that the value of the temperature is increased according to the increase in the fuel mass flow. Therefore, in the figure below, the maximum value of the mixture fraction is increased too, so this means that more fuel is added in the mixture.

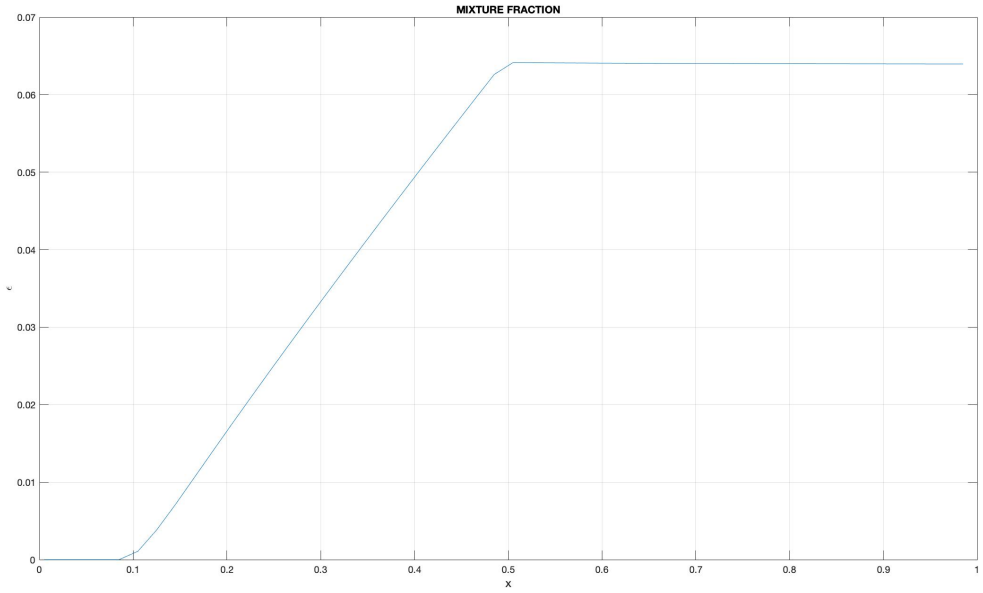

Figure 4.10. Mixture fraction through the combustion chamber and the nozzle by adding the thermal model

The figure below represents the mole fractions of the considered chemical species; it is evident that the oxygen mole fraction reaches a lower value than that reached in the previous simulation. This was to be expected according to the mixture fraction, more fuel is added more oxygen is consumed.

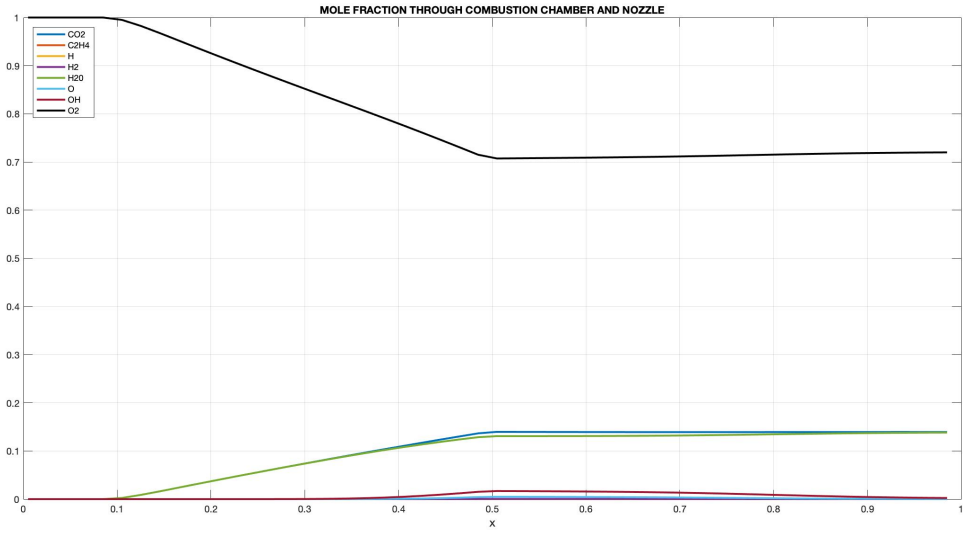

Figure 4.11. Mole fractions through the combustion chamber and the nozzle by adding the thermal model

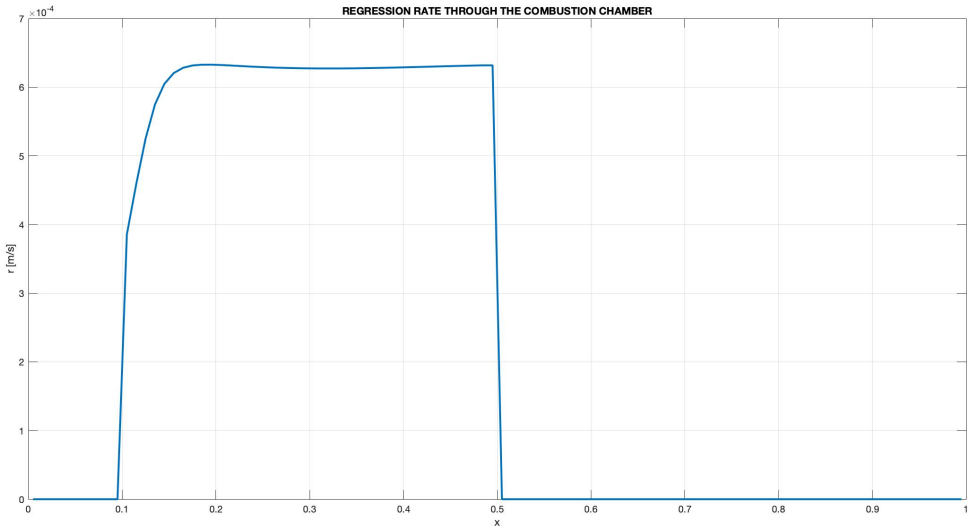

Figure 4.12. Regression rate through the combustion chamber and the nozzle by adding the thermal model

In the last graph exposed, the regression rate through the combustor is shown. This value is equal to zero before $x = 0.1$ and after $x = 0.5$, because the fuel injection was imposed to happen inside that region. Furthermore, the value reached is almost constant inside that region and is equal to $\dot{r} \cong 6.5d - 4 \left[\frac{m}{s}\right]$. This trend is what I expected, because the boundary time delay is set equal to zero and the instability phenomena do not appear.

4.5 Pressure and regression rate history with and without the boundary layer delay time

The last graphs showed the pressure and the regression rate, with $\tau_{BL} = 0\ [s]$, through the combustion chamber. In order to focus the attention into the time signal and to appreciate the pressure and regression rate oscillations, I chose to track these two variables in $x = 0.3$, which corresponds to the middle of the combustor. Firstly the boundary layer delay time was set to zero and the results are represented in the figure below.

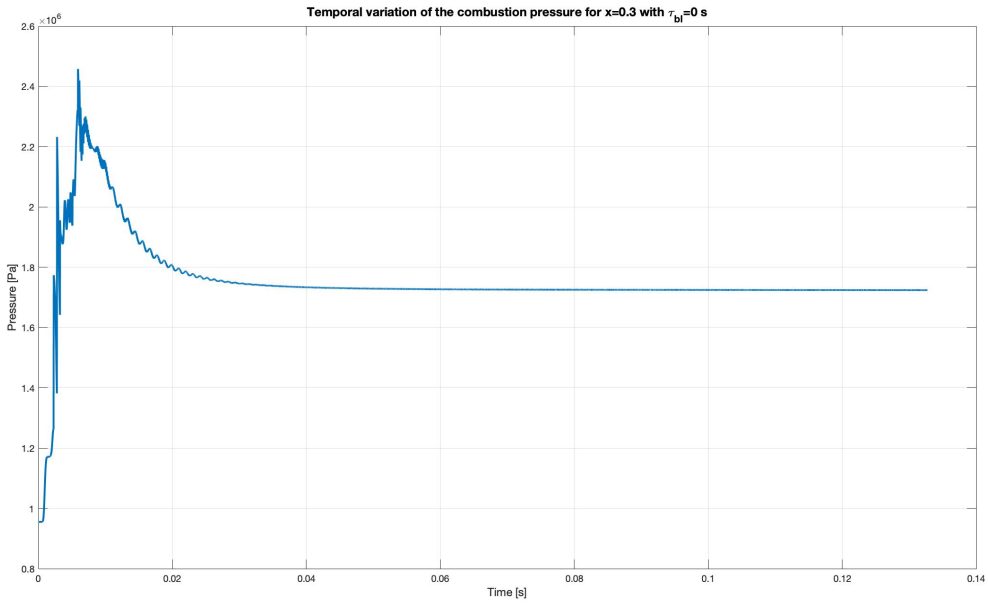

Figure 4.13. Temporal variation of the pressure in $x = 0.3$ and with $\tau_{BL} = 0\ s$

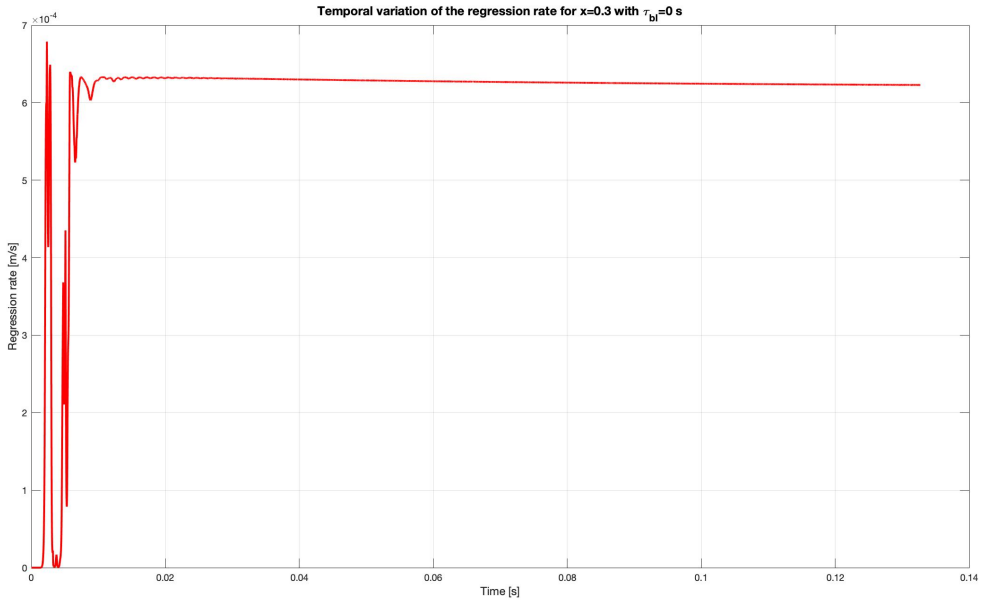

Figure 4.14. Temporal variation of the regression rate in $x = 0.3$ and with $\tau_{BL} = 0\ s$

Despite the short time of the simulation, it is evident that the system has reached his steady state condition because both the pressure and the regression rate, after a sharp transitional period, do not present any oscillations. Different is the case with boundary layer delay time set equal to one millisecond $\tau_{BL} = 0\ .001[s]$.

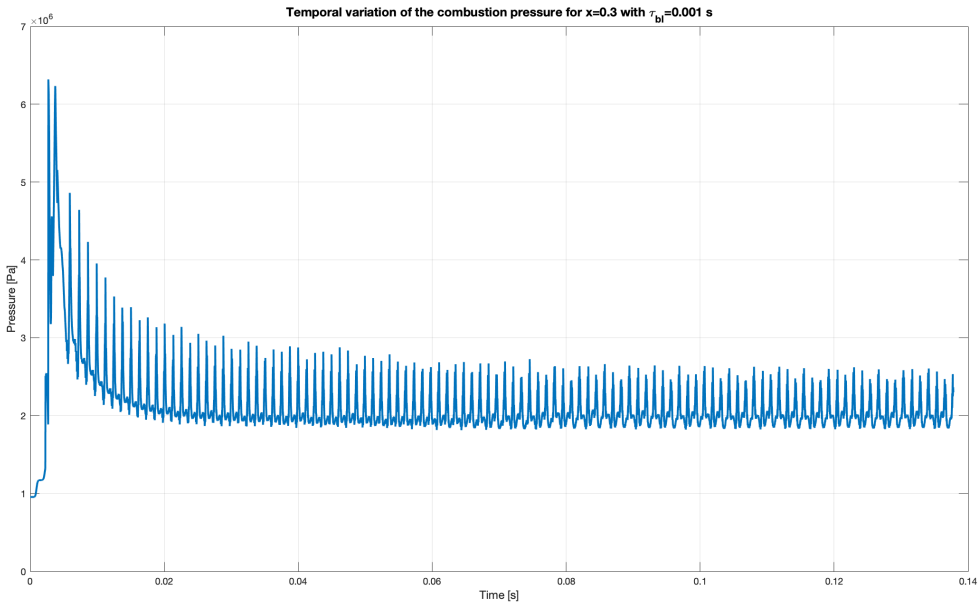

Figure 4.15. Temporal variation of the pressure in $x = 0.3$ and with $\tau_{BL} = 0.001\ s$

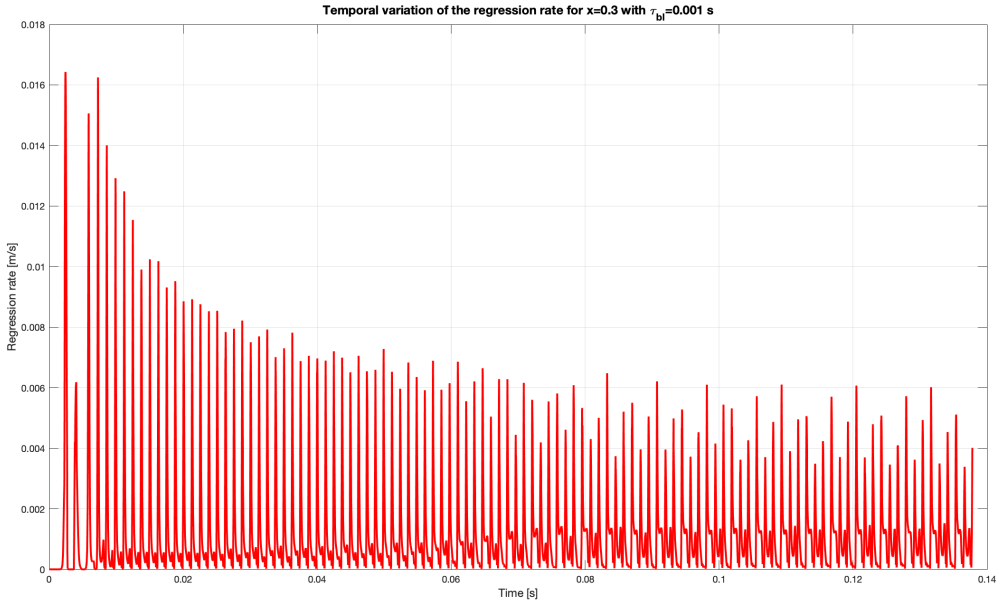

Figure 4.16. Temporal variation of the regression rate in $x = 0.3$ and with $\tau_{BL} = 0.001\ s$

Even if the small value of τ_{BL}, the oscillations are evident. The goal of this numerical code is that the oscillations in the regression rate can be translated in terms of pressure oscillations. Given that, the boundary layer delay time is the delay between the wall heat flux and the response of the regression rate, this leads to the oscillations in this parameter, but there is not a relation that links it with the pressure. Indeed, as I wrote before, the regression rate in the HREs is linked to the mass flux; as a consequence, the CFD code is able to appreciate the changes in the mass flux, in detail in the fuel mass flux,

and to convert them in pressure oscillations. It is worth noting that, in the figure 4.15, the so-called “DC shift” in the chamber pressure is present and the oscillation proceeds into a nonlinear limit cycle.

Conclusion

The goal of this thesis is to develop a numerical code that is able to analyse the transient phenomena and to catch the instability due to the boundary layer delay time. Firstly, it was necessary to split the physical models that took place in this analysis, there are the quasi-one-dimensional gas dynamic model, the chemical model and the one-dimensional thermal model. Then, every model was discretized by an appropriate numerical method; as regards the chemical model, the CEA code was used together with a further code, this one was developed in this thesis and it is able to substitute the CEA code when the assumption that the mole fractions are constant is acceptable. This additional code enables to reduce the computational time. For the other two physical models, the Finite Volume Method was used. Furthermore, in the Q1D gas dynamic model, a further equation was needed so as to take into account the presence of the fuel mass through the mixture fraction ϵ. Specific attention has been taken for the fluxes discretization and for the boundary condition; the Lax-Friedrichs method was used for the fluxes, but it was slightly modified in order to take γ and $\tilde{R}$ as inputs, because with the presence of the chemical reaction these two parameters are also variables between two adjacent cells. Indeed, the boundary condition at the inlet, in the nozzle geometry case, was adjusted in such a way that the chemical contribution, in the specific internal energy, would be considered. This was possible by introducing a *"bias"*, so as to make coherent the internal energy evaluated from the CEA code, through a polynomial fitting, and the internal energy evaluated from the characteristics equations used in the boundary condition for subsonic flow. In the thermal model, special attention, was taken in the domain discretization, as it was explained in the chapter 4.3, and in the wall heat flux. This last one depends on the oxidizer mass flux and the regression rate; furthermore, two relations were implemented, based on the blowing parameter according to [17]. Anyway, in the chapter 3 a more detailed explanation of the numerical method can be found.

Finally these four numerical codes were linked together after a validation of each coupling as it can be seen in the chapter 4. In the paragraph 4.4 the final results are exposed and in the paragraph 4.5 the difference between $\tau_{BL} = 0\ s$ and $\tau_{BL} = 0.001\ s$ is shown. In addition, it was noted that the instability takes place when the boundary layer delay time is present.

As a conclusion, this numerical code shows good results although the approximations made. Future works will be done to improve the code both in the numerical method and in the physical model.

Bibliography

[1] Chiaverini, M., J., "Fundamentals of Hybrid Rocket Combustion and Propulsion," *American Institute of Aeronautics and Astronautics*, Vol. 218, 2007, pp. 1-36

[2] Zak, A., "Jar of jelly: Origin of Vehicle 09," in http://www.russianspaceweb.com/gird09.html

[3] Ewing, E. G. Journal of the Pacific Rocket Society , 1947.

[4] Moore, G. E., and Berman, K. "A Solid Liquid Rocket Propellant System," Jet Propulsion, Vol. 26, No. 11, 1956.

[5] Valdes, R., "How SpaceShipOne Works," in https://science.howstuffworks.com/spaceshipone8.htm

[6] Drees K., "The Sky IS NOT the Limit!," in https://www.csda.net/blogs/csda-admin/2019/11/05/the-sky-is-not-the-limit

[7] David, L., "SpaceShipOne Wins $10 Million Ansari X Prize in Historic 2nd Trip to Space," in https://www.space.com/403-spaceshipone-wins-10-million-ansari-prize-historic-2nd-trip-space.html

[8] Howell, E., "SpaceShipTwo: On a Flight Path to Space Tourism," in https://www.space.com/19021-spaceshiptwo.html

[9] Boyle, A., "Virgin Galactic Makes a Switch in SpaceShip Two's Rocket Motor," in https://www.nbcnews.com/storyline/virgin-voyage/virgin-galactic-makes-switch-spaceshiptwos-rocket-motor-n113216

[10] Foust, J., "SpaceShipTwo Bounces Back to Rubber Fuel," in https://spacenews.com/virgin-galactic-switching-back-to-rubber-fuel-for-spaceshiptwo/

[11] Karthikeyan, G., and Shimada, T., "Numerical Parametric Analysis of Combustion Instability in Axial-Injected Hybrid Rocket Motors," *Journal of Propulsion and Power*

[12] Pastrone, D., "Approaches to Low Fuel Regression Rate in Hybrid Rocket Engines," *International Journal of Aerospace Engineering*, Hindawi Publishing Corporation, Volume 2012, Article ID 649753

[13] Karabeyoglu, M. A., Cantwell, B. J., and Altman, D., "Develop- ment and testing of paraffin-based hybrid rocket fuels," in *Pro- ceedings of the 37th AIAA/ASME/SAE/ASEE Joint Propulsion Conference and Exhibit*, July 2001, AIAA Paper 2001-4503.

[14] Karabeyoglu, M. A., De Zilwa, S., Cantwell, B., Zilliac, G., "Modeling of Hybrid Rocket Low Frequency Instabilities," *Journal of Propulsion and Power*, Vol. 21, No. 6, November-December 2005

[15] Park, K. S., and Lee, C., "Low frequency instability in laboratory-scale hybrid rocket motors," *Aerospace Science and Technology*, Volume 42, 2015

[16] Gordon, S., and McBride, B. J., "Computer Program for Calculation of Complex Chemical Equilibrium Compositions and Applications," *NASA Reference Publication 1311,* October 1994

[17] Pastrone, D., and Carmicino, C., "On the Explanation of the "DC Shift" in Hybrid Rockets," *AIAA Propulsion and Energy Forum*, July 9-11, 2018

[18] Marxman, G. A. and Gilbert, M., "Turbulent boundary layer combustion in the hybrid rocket," *Ninth International Symposium on Combustion*, Academic Press, New York, 1963, pp. 371-383

[19] Marxman, G. A., "Combustion in the turbulent boundary layer on a vaporizing surface," *Symposium (International) on Combustion*, Volume 10, Issue 1, 1965

[20] LeVeque, R. J., "Finite Volume Method for Hyperbolic Problems," Cambridge Texts in Applied Mathematics, Volume 31, in Cambridge University Press, August 26, 2002

[21] Blazek, J., "Computational Fluid Dynamics : Principles and Applications," *Elsevier Science & Technology*, 2005

[22] Gordon, S., and McBride, B. J., "Computer Program for Calculation of Complex Chemical Equilibrium Compositions and Applications," *NASA Reference Publication 1311,* June 1996

[23] Eschenroeder et al., "Shock Tunnel Studies of High-Enthalpy Ionized Airflows," Cornell Aeronautical Lab., Rept. AF-1500 A1, Buffalo, NY, 1962

[24] Zilliac, G., and Karabeyoglu, M. A., " Hybrid Rocket Fuel Regression Rate Data and Modeling," *42nd AIAA/ASME/SAE/ASEE Joint Propulsion Conference & Exhibit,* 9-12 July 2006, Sacramento, California